TITLE

Optogenetic Miro cleavage reveals direct consequences of real-time loss of function in *Drosophila*.

Francesca Mattedi[1], Ethlyn Lloyd-Morris[1], Frank Hirth[1], and Alessio Vagnoni[1#].

[1]Department of Basic and Clinical Neurosciences, Maurice Wohl Clinical Neuroscience Institute, Institute of Psychiatry, Psychology and Neuroscience, King's College London, 5 Cutcombe Road, London, SE5 9RX, UK

[#]Correspondence to: alessio.vagnoni@kcl.ac.uk

ABSTRACT

Miro GTPases control mitochondrial morphology, calcium homeostasis and regulate mitochondrial distribution by mediating their attachment to the kinesin and dynein motor complex. It is not clear, however, how Miro proteins spatially and temporally integrate their function as acute disruption of protein function has not been performed. To address this issue, we have developed an optogenetic loss of function 'Split-Miro' allele for precise control of Miro-dependent mitochondrial functions in *Drosophila*. Rapid optogenetic cleavage of Split-Miro leads to a striking rearrangement of the mitochondrial network, which is mediated by mitochondrial interaction with the microtubules. Unexpectedly, this treatment did not impact the ability of mitochondria to buffer calcium. While Split-Miro overexpression is sufficient to augment mitochondrial motility, sustained photocleavage shows Split-Miro is surprisingly dispensable to maintain elevated mitochondrial processivity. Furthermore, functional replacement of endogenous Miro with Split-Miro identifies its essential role in the regulation of locomotor activity in adult flies, demonstrating the feasibility of tuning animal behaviour by real-time loss of protein function.

INTRODUCTION

Methods to observe loss of function (LoF) phenotypes are used to study many biological processes. Although important tools for elucidating gene function, disruption of genes by genomic mutations or RNA interference often does not have the spatio-temporal resolution to capture the direct cellular and organismal consequences of LoF and to report specifically on a protein's primary function. The observed 'end-point' phenotypes might thus be the result of compensatory mechanisms to loss of protein, and gene pleiotropy means that, even in cell culture models, it is often difficult to dissect the causality of the observed phenotypes.

This issue is especially problematic when studying complex cellular processes such as mitochondrial dynamics, and it is particularly evident for Miro proteins, mitochondrial Rho GTPases that influences the motility, morphology and physiology of mitochondria (Eberhardt et al., 2020; Reis et al., 2009; Lee and Lu, 2014). In *Drosophila*, homozygous mutants of *miro* are developmentally lethal (Guo et al., 2005) while knockout of *Miro1* in mice leads to perinatal lethality (Nguyen et al., 2014; López-Doménech et al., 2018). Chronic loss of Miro is detrimental for mitochondrial transport in *Drosophila* and mammalian neurons (Russo et al., 2009; MacAskill et al., 2009; Wang and Schwarz, 2009), where it leads to alteration of synaptic strength (Guo et al., 2005; Vaccaro et al., 2017) whereas disruption of Miro in *Drosophila* additionally impairs mitochondrial calcium homeostasis (Li et al., 2021; Lee et al., 2016). Reducing Miro abundance has also profound effects on mitochondrial morphology with fragmented mitochondria observed in yeast (Frederick et al., 2004), *Drosophila* larval motor neurons (Russo et al., 2009) and mouse embryonic fibroblasts (López-Doménech et al., 2018). It is not yet clear, however, to what extent these phenotypes are directly consequences of Miro disruption and whether they might arise independently. Any attempt to dissect the causality of cellular and organismal phenotypes after Miro manipulation is challenging as the current tools do not allow acute disruption of function.

Here we present the generation of 'Split-Miro', a photocleavable variant of *Drosophila* Miro, to achieve rapid and controlled loss of protein function. Mitochondrial network remodelling is a rapid response to Split-Miro photocleavage in *Drosophila* S2R+ cells. This effect, mediated by loss of anchorage to the microtubule network, impacts on

mitochondrial distribution into cell processes where the use of Split-Miro shows that this protein is sufficient to increase mitochondrial motility but dispensable for the maintenance of elevated mitochondrial velocities. Unexpectedly, we show that Split-Miro photocleavage does not directly impact mitochondrial calcium homeostasis. Finally, we demonstrate that Split-Miro rescues the lethality associated with classical Miro LoF mutations when expressed in the fly nervous system and that this affords control of fly locomotor activity through exposure to blue light. To our knowledge, this is the first example of tuneable animal behaviour by real-time loss of protein function.

RESULTS

Design of a photocleavable Miro variant in Drosophila.

To gain real-time spatio-temporal control of Miro LoF, we created a Miro variant that contains the LOV2-Zdk1 protein pair (Fig. 1A-B) that undergoes light-induced dissociation upon exposure to blue light (Wang et al., 2016; Van Haren et al., 2018; Dema et al., 2022) and so is predicted to achieve rapid and reversible Miro LoF through protein photocleavage (Fig. 1B).

We fused Zdk1 N-terminally to the mitochondrial targeting transmembrane domain of Miro, with LOV2 fused C-terminally to the rest of the protein (Fig. 1A-B), and expressed this optogenetic variant of Miro (herein called ‘Split-Miro’) as two components in *Drosophila* S2R+ cells (Fig. 1B-C). In absence of blue light, LOV2 interacts with Zdk1 thus reconstituting Split-Miro at the mitochondria (Fig. 1C). However, upon blue light exposure, the LOV2 Jα helix undergoes a conformational change that prevents Zdk1 from binding (Van Haren et al., 2018; Wang et al., 2016), resulting in the photocleavage of Split-Miro and the rapid release of the N-terminal moiety into the cytoplasm (Fig. 1D, Movie 1). Quantifications of the kinetics of release after blue light exposure showed release half-life of 1.4 ± 0.9 seconds (Fig. 1E, Supplementary Fig. 1A-B) and full Split-Miro reconstitution within 2 minutes (Fig. 1F, Supplementary Fig. 1A,C) after removal of blue light, in line with what was previously reported for the LOV2-Zdk1 association in mammalian cells (van Haren et al., 2020; Wang et al., 2016).

Overexpression of Split-Miro increases the proportion of motile mitochondria and their processivity in cell processes.

Drosophila S2R+ cells are often used for intracellular trafficking experiments (Ally et al., 2009; Vagnoni et al., 2016) and can be induced to extend processes (Fig. 2A) with a stereotypical plus-end out microtubule array (Jolly et al., 2016; Vagnoni et al., 2016) that display Miro-dependent long-range, bidirectional mitochondrial motility (Fig. 2B-D, Supplementary Fig. 2A-C). With the aim of studying whether mitochondrial motility can be manipulated via Split-Miro, we first transfected S2R+ cells with either Split-Miro or wild-type Miro (wt-Miro) N-terminally tagged with mCherry. We initially exploited the mCherry tag to follow mitochondria with a 561-nm laser line, which does not photocleave Split-Miro (Fig. 2E-G, 561-nm laser).

Miro links kinesin and dynein motors to mitochondria via milton (TRAK1/2 in mammals) (MacAskill et al., 2009; Wang and Schwarz, 2009; van Spronsen et al., 2013; Brickley and Stephenson, 2011; Glater et al., 2006; Fransson et al., 2006) (Supplementary Fig. 2D-E) and so overexpression of Miro is predicted to favour the recruitment of motor proteins on mitochondria for processive transport. Consistent with this idea, mitochondria spent more time on long runs, paused less and engaged less frequently in short runs after either Miro or Split-Miro overexpression compared to controls (Fig. 2F, 561-nm laser, Supplementary Fig. 2F-G). Thus, both Miro isoforms turn the motility of mitochondria from predominantly bidirectional with frequent reversals to markedly more processive. Further supporting this notion, both Miro isoforms caused a higher proportion of mitochondria in cells processes to be motile (Fig. 2G, 561-nm laser) and their duty cycle increased in both the anterograde and retrograde directions (Supplementary Fig. 1H), suggesting that Miro participates in the activation of transport complexes for bidirectional mitochondrial transport. Interestingly, while there was no difference in the retrograde run velocities when Miro or Split-Miro were overexpressed, mitochondria traveling in the anterograde direction moved at nearly double the speed when compared to control (Fig. 2H, 561-nm laser). This observation might reflect a preference for Miro to recruit milton-kinesin complexes, consistent with what was observed in larval segmental neurons after Miro overexpression (Liu et al., 2012). Collectively, these experiments shed light on Miro's role in regulating mitochondrial motility in S2R+ cells and demonstrate that, in absence of blue light exposure, Split-Miro and Miro are functionally equivalent.

Optogenetic cleavage of Split-Miro reduces the proportion, but not the processivity, of motile mitochondria in the cell processes.

To test whether Split-Miro photocleavage reverses the observed Miro gain-of-function effects on mitochondrial transport, we analysed mitochondrial motility under blue light in wt-Miro and Split-Miro transfected cells. Time-lapse imaging with the 488-nm laser line ensured Split-Miro was not reconstituted while recording mitochondrial motility via the EGFP-tag (Fig. 2E, green). wt-Miro, which cannot be photocleaved, was used as a control. We found that while there was no detectable difference in the motility after imaging for one minute (Supplementary Data Fig. 2I), sustained Split-Miro photocleavage (7 minutes) reduced the time mitochondria spent on long runs and the proportion of organelles in the processes that were motile to the levels observed prior to overexpression, while there was no such effect in wt-Miro controls (Fig. 2E-G, 488-nm laser). Cleaving Split-Miro from mitochondria did not, however, have any major effects on the velocity and run length of the moving organelles, which remained elevated and did not return to control levels (Fig. 2H, 488-nm laser, Supplementary Fig. 2J). This was also the case when endogenous Miro was depleted in the Split-Miro condition by RNAi (Supplementary Fig. 2K). Thus, these results indicate that the proportion and processivity of motile mitochondria are controlled by separate Miro-dependent and Miro-independent mechanisms.

Split-Miro photocleavage triggers a rapid collapse of the mitochondrial network which is rescued by mitochondrial anchoring to the microtubules.

We next examined the effect of Split-Miro on the integrity of the mitochondrial network in the cell soma. Strikingly, exposing Split-Miro-transfected S2R+ cells to blue light triggered a rapid (< 3 min) and dramatic remodelling of the entire mitochondrial network which progressively collapsed towards the centre of the cell (Fig. 3A, Movie 2). Mitochondria shortened along their long axis taking up a rounder shape (Fig. 3B), which was associated with a strong reduction in the number of branches (Fig. 3C) and reduction of the total area covered by mitochondria (Supplementary Fig. 3A). Again, the presence of endogenous Miro was dispensable for Split-Miro functionality as reducing Miro levels by RNAi did not affect the mitochondrial phenotype in Split-Miro-transfected cells (Fig. 3D). Of note, neither the distribution of peroxisomes in the cell processes (Supplementary Fig. 3B) nor the overall organisation of the microtubule network (Supplementary Fig. 3C) was affected by this rapid cellular-scale change. Nevertheless,

we reasoned that mitochondrial network collapse might impede organelle delivery towards the periphery. The number of mitochondria in the cell processes showed a progressive decline in mitochondrial content in cells expressing Split-Miro under blue light, while no effect was observed in the presence of wt-Miro (Supplementary Fig. 3D-E). We conclude that the rapid mitochondrial shape transition with associated loss of network integrity, clearly detectable within 3 minutes under blue light, strongly contributes to the progressive depletion of mitochondria from the cell processes.

The Miro-milton-motor complex provides a link for the attachment of mitochondria onto the microtubules (Nemani et al., 2018; Chung et al., 2016). To test the hypothesis that loss of microtubule tethering is responsible for the collapse of the mitochondrial network, we set out to induce mitochondrial tethering to the microtubules in a Miro-independent manner. In mammals, syntaphilin (SNPH) anchors mitochondria onto the microtubules (Kang et al., 2008), although a *Drosophila* homologue has not yet been found. Thus, we co-expressed EGFP-tagged human SNPH with Split-Miro in S2R+ cells stained with MitoTracker. SNPH signal in *Drosophila* cells overlaps with mitochondria and, as observed in mammalian neurons, SNPH puncta often localise at mitochondrial ends and are associated with strong reduction in mitochondrial dynamics (Fig. 3E-E', Supplementary Fig. 3F-G). While in cells devoid of SNPH the mitochondrial network retracts after Split-Miro photocleavage, the presence of SNPH prevents this phenotype (Fig. 3E-G). These observations support the notion that loss of mitochondrial anchoring on microtubules is responsible for the rapid mitochondrial network collapse when Split-Miro is cleaved.

Split-Miro photocleavage does not affect mitochondrial calcium buffering.

Mitochondria buffer calcium to help maintain cellular homeostasis and loss of Miro reduces calcium levels in the mitochondria of the *Drosophila* brain (Lee et al., 2016, 2018; Li et al., 2021). However, the mechanisms underlying decreased calcium uptake when Miro is disrupted are not understood. In S2R+ cells, Split-Miro photocleavage did not induce any changes in the fluorescent intensity of the mitochondrial calcium $[Ca^{2+}]_m$ indicator mito-GCaMP6f when compared to control cells (Fig. 4A-B), indicating that the steady-state level of $[Ca^{2+}]_m$ is not affected by this manipulation. Optogenetic inactivation of Split-Miro also did not affect $[Ca^{2+}]_m$ uptake when S2R+ cells were challenged with ionomycin, an ionophore that causes a sharp increase in cytosolic

calcium (Nemani et al., 2018; Niescier et al., 2018) (Fig. 4C-E). This result indicates that the mitochondrial morphological changes induced by Split-Miro are not sufficient to alter $[Ca^{2+}]_m$ homeostasis. Likewise, overexpression of SNPH, which rescues the Split-Miro-induced mitochondrial collapse, did not have any effect on $[Ca^{2+}]_m$ uptake when Split-Miro was cleaved (Fig. 4C-E). Furthermore, the morphological changes displayed by mitochondria after Split-Miro photocleavage were not associated with detectable changes in their membrane potential (Supplementary Fig. 4), implying that mitochondria do not become dysfunctional during this rapid morphological transition. Together these findings suggest that acutely modulating mitochondrial network integrity via Split-Miro/SNPH or blocking mitochondrial motility via SNPH (Supplementary Fig. 3F-G) are not sufficient to perturb $[Ca^{2+}]_m$ homeostasis in this context.

Inducible and age-dependent hyperactivity of Split-Miro flies.

Genetic mutations and RNAi have shown that Miro is critical for mitochondrial functionality in the nervous system (MacAskill et al., 2009; Russo et al., 2009; Nguyen et al., 2014). Homozygous *miro* gene loss of function alleles are lethal, thus precluding a comprehensive analysis of Miro function in adult animals. Conditional loss of Miro1 in mouse neurons causes severe movement defects within 30 days post-natal (Nguyen et al., 2014) and both increased and reduced Miro abundance in the *Drosophila* nervous system can rescue fly climbing activity in models of neurodegeneration(Panchal and Tiwari, 2020; Shaltouki et al., 2018). These findings suggest that real-time Miro disruption in the adult nervous system could be exploited to manipulate animal behaviour.

We turned to behavioural genetics to assess Split-Miro versatility for the study of organismal phenotypes. Pan-neuronal expression of UAS-mCherry-MiroN-LOV2 and UAS-Zdk1-MiroC (herein, 'UAS-Split-Miro') with the *Appl-Gal4* driver rescued the lethality associated with classic null mutations of the Miro gene ($miro^{Sd32/B682}$) (Fig. 5A, Supplementary Fig. 5A). Adult flies were assayed for their motor behaviour at day 2 and day 8 before, during and after blue-light exposure using the 'Opto-DART' system (Fig. 5B). Split-Miro could be reconstituted in adult fly neurons *in vivo* and can be photocleaved efficiently through exposure to blue light (Supplementary Fig. 5B-D). $miro^{Sd32/B682}$, *UAS-Split-Miro* flies at 2 days of age showed a modest increase in locomotor activity after an hour of exposure to blue light, which was sustained also after

the exposure to light ceased (Fig. 5C-E). These observations suggest that the effects of Split-Mito photocleavage were not rapidly reversed after removal of blue-light.

Strikingly, 8 days-old *miro*$^{Sd32/B682}$, *UAS-Split-Miro* flies displayed a rapid and sustained increase in motor activity when exposed to blue light compared to control, while no difference was observed in their baseline activity prior to exposure to blue light (Fig. 5F-H). While the fly speed returned to control level as the blue light was turned off, the action initiation revealed a prolonged effect on locomotor activity, similar to what observed in younger flies (Fig. 5F-H). Remarkably, Split-Miro-dependent effects on fly activity and action initiation could be reversed by co-expressing human SNPH (UAS-SNPH) with *Appl-Gal4* (Fig. 5I-K). Thus, SNPH can also suppress the effect of Miro inactivation in the context of animal behaviour. Together, these results show that acute loss of Miro function leads to fly hyperactivity, and this phenotype is exacerbated by ageing and suppressed by expression of SNPH. Collectively, these experiments reveal that Split-Miro is effective in an adult animal and uncover a previously unknown role of Miro in the regulation of *Drosophila* locomotor behaviour.

DISCUSSION

Using optogenetics to implement a real time LoF paradigm by targeting Miro, we show that collapse of the mitochondrial network is an immediate response to Miro photocleavage in S2R+ cells which temporally precedes the defects observed in mitochondrial trafficking. We found that Miro overexpression increases the proportion and the processivity of mitochondria transported in the processes of S2R+ cells. Surprisingly, although sustained Split-Miro photocleavage reverted the proportion of transported mitochondria to control levels, the velocities and run lengths of the motile organelles were largely unaffected. This scenario is consistent with an essential role for Miro in the recruitment of transport complexes for activation of bidirectional transport, likely by recruiting (Fenton et al., 2021; Henrichs et al., 2020) or directly activating (Canty et al., 2021) molecular motor complexes. However, we hypothesise that once motors have been recruited onto mitochondria, they may link to the organelles via additional factors in a Miro-independent way, at least on a proportion of mitochondria (Fig. 6). Future studies should focus on discovering these factors, for example by

testing if the functional homologs of metaxins (Zhao et al., 2021) in *Drosophila* could fulfil this role.

Rapid retraction of the mitochondrial network in the cell soma after Split-Miro photocleavage is conceivably a consequence of releasing membrane tension that accumulates under stretch, reminiscent of the recoil of daughter mitochondria after fission (Mahecic et al., 2021). Increased mitochondrial tension following Miro overexpression is consistent with the idea that more motors are recruited and pull onto the mitochondrial membrane via cytoskeletal interaction (Helle et al., 2017; Song et al., 2022; König et al., 2021; Qin et al., 2020), which would likely contribute to the build-up of mechanical energy onto an interconnected network. According to this view, releasing the link between mitochondria and the microtubules then triggers the rapid collapse of the network. It would be interesting in future investigations to establish whether the phenotype that we observe could be regarded as a 'mitoquake', i.e. rapid mitochondrial network disruption with associated release of mechanical energy, similar to the sudden cytoskeletal rearrangements ('cytoquakes') that were proposed to underpin mechanical adaptivity during cellular dynamic processes (Floyd et al., 2021).

We found that using SNPH to tether mitochondria onto the microtubule network prevented Split-Miro-induced mitochondrial reorganisation, indicating that Miro stabilises the mitochondrial network by providing an anchor to the cytoskeleton. It is possible, however, that Miro may stabilise the mitochondrial network by simultaneously bridging mitochondria to different cellular structures. In this regard, we did not find that the actin cytoskeleton plays a significant role in S2R+ cells (Supplementary Fig. 2). It is conceivable that the actin network contributes to mitochondrial stability via Miro-Myosin interactions in other cell types (Oeding et al., 2018; López-Doménech et al., 2018). It has been shown that a subset of Miro is found at the mitochondria-ER interface to regulate the contacts between these two organelles (Modi et al., 2019; Guillén-Samander et al., 2021). Testing whether Miro-dependent mitochondrial interaction with the ER and other cellular structures is necessary to maintain mitochondrial network stability is a goal for future studies.

Decreasing the abundance of Miro by RNAi reduced $[Ca^{2+}]_m$ levels in the neurons of *Drosophila* brain (Lee et al., 2016; Li et al., 2021) and mutating the Ca^{2+}-binding EF

domains of Miro reduced $[Ca^{2+}]_m$ uptake in mouse hippocampal neurons (Chang et al., 2011), although Miro1-KO and Miro-EF mutant MEFs did not show any disturbances in $[Ca^{2+}]_m$ homoeostasis (Nguyen et al., 2014; Nemani et al., 2018). In S2R+ cells, shedding Split-Miro functional domains (including the Ca^{2+}-binding EF-hands motifs) did not have any effect on $[Ca^{2+}]_m$ uptake. We hypothesise that impaired $[Ca^{2+}]_m$ homeostasis shown with classical Miro LoF approaches (i.e., RNAi, knock-out) may be a secondary effect of Miro LoF, potentially a consequence of sustained morphological and transport defects of mitochondria. Overexpressing SNPH to rescue Split-Miro-dependent mitochondrial network retraction also did not affect $[Ca^{2+}]_m$ uptake. Because SNPH also locks mitochondria into a stationary state with little network dynamic, these results raise the intriguing possibility that mitochondrial movements are not critical to maintain $[Ca^{2+}]_m$ homeostasis, as long as mitochondria maintain their functionality.

Elegant methods for light-induced repositioning of trafficked vesicles and mitochondria have been developed which are based on the recruitment of truncated forms of motor proteins to overpower the endogenous transport machinery and so to achieve controlled redistribution of cellular cargoes (van Bergeijk et al., 2015; Ballister et al., 2015; Gutnick et al., 2019; Harterink et al., 2016). Engineering the LOV2-Zdk1 domain into subunits of motor and adaptor proteins could offer a complementary strategy for studying intracellular trafficking when a real-time LoF approach is preferred. Because protein photocleavage is reversible, the LOV2-Zdk1 methodology also offers significant advantages over existing methods based on the rapid, non-reversible, degradation of a target protein by the proteasome, such as the degron (Yesbolatova et al., 2020) or the TRIM-away systems (Clift et al., 2017).

Opsin-based optogenetic approaches to activate/repress specific neurons and study associated animal behaviour have been extensively used in live animals (Deubner et al., 2019). A LOV2-controlled CaMKII inhibitor was used to impair memory formation in live mice after blue-light stimulation for 1 hour (Murakoshi et al., 2017). By creating Split-Miro flies, we combine optogenetics with *Drosophila* behaviour and neuronal specificity to perform LoF experiments in adult animals in real time. Although the locomotor behaviour of Split-Miro flies is indistinguishable from the wild-type counterpart before exposure to blue light, their activity is enhanced under blue light and this hyperactivity becomes more pronounced with age. The remarkable rescue of fly

hyperactivity by SNPH overexpression points to an important role of neuronal mitochondrial mobility for animal behaviour.

It is conceivable that Split-Miro triggers an acute imbalance of neuronal homeostasis and synaptic transmission, which leads to augmented locomotor activity. In line with this notion, reducing mitochondrial number positively correlates with activity-dependent vesicular release at the presynapses of hippocampal and cortical neurons (Vaccaro et al., 2017; Kwon et al., 2016) and with miniature excitatory junction potentials at the *Drosophila* NMJ (Guo et al., 2005). Moreover, ageing has been associated with increased activity of excitatory neurons in *C. elegans*, flies and mice (Zullo et al., 2019; Simkin et al., 2015; Haberman et al., 2017; Wong et al., 2021). Our data suggest that Miro could play a crucial role in preventing hyperexcitation in the ageing nervous system with potential ramification in the context of neurodegeneration.

ACKNOWLEDGMENTS

We thank Tito Calì, Manolis Fanto, Gohta Goshima, Marc-David Ruepp, Tom Schwarz, Zu-Hang Sheng, Konrad Zinsmaier and Alex Whitworth for sharing reagents, the Fly Facility of the Department of Genetics, University of Cambridge for help with *Drosophila* embryo injections, the BFK Lab Ltd for assistance with the behavioural assays, the Wohl Cellular Imaging Centre at King's College London for help with light microscopy, and the Bloomington Drosophila Stock Center for fly stocks. We thank members of the Vagnoni lab, Joe Bateman and Simon Bullock for critically reading the manuscript. The work was supported by an NC3Rs David Sainsbury fellowship and Skills and Knowledge Transfer grant (NC/N001753/2 and NC/T001224/1), an Academy of Medical Sciences Springboard Award (SBF004/1088), a van Geest Fellowship in Dementia and Neurodegeneration and van Geest PhD studentship awards to A.V, and by the Alzheimer's Research UK London Network Centre grant. The authors declare no competing financial interests.

REFERENCE LIST

Ally, S., A.G. Larson, K. Barlan, S.E. Rice, and V.I. Gelfand. 2009. Opposite-polarity motors activate one another to trigger cargo transport in live cells. *J. Cell Biol.*

187:1071–1082. doi:10.1083/JCB.200908075.

Babic, M., G.J. Russo, A.J. Wellington, R.M. Sangston, M. Gonzalez, and K.E. Zinsmaier. 2015. Miro's N-terminal GTPase domain is required for transport of mitochondria into axons and dendrites. *J. Neurosci.* 35:5754–71. doi:10.1523/JNEUROSCI.1035-14.2015.

Ballister, E.R., S. Ayloo, D.M. Chenoweth, M.A. Lampson, and E.L.F. Holzbaur. 2015. Optogenetic control of organelle transport using a photocaged chemical inducer of dimerization. *Curr. Biol.* 25:R407–R408. doi: 10.1016/j.cub.2015.03.056

van Bergeijk, P., M. Adrian, C.C. Hoogenraad, and L.C. Kapitein. 2015. Optogenetic control of organelle transport and positioning. *Nature*. 518:111–114. doi:10.1038/nature14128.

Brickley, K., and F.A. Stephenson. 2011. Trafficking kinesin protein (TRAK)-mediated transport of mitochondria in axons of hippocampal neurons. *J. Biol. Chem.* 286:18079–92. doi:10.1074/jbc.M111.236018.

Canty, J.T., A. Hensley, and A. Yildiz. 2021. TRAK adaptors coordinate the recruitment and activation of dynein and kinesin to control mitochondrial transport. *bioRxiv*. doi:10.1101/2021.07.30.454553.

Chang, K.T., R.F. Niescier, and K.-T. Min. 2011. Mitochondrial matrix Ca2+ as an intrinsic signal regulating mitochondrial motility in axons. *Proc. Natl. Acad. Sci. U. S. A.* 108:15456–61. doi:10.1073/pnas.1106862108.

Chaudhry, A., R. Shi, and D.S. Luciani. 2020. A pipeline for multidimensional confocal analysis of mitochondrial morphology, function, and dynamics in pancreatic β-cells. *Am. J. Physiol. Endocrinol. Metab.* 318:E87–E101. doi:10.1152/ajpendo.00457.2019.

Chung, J.Y.M., J.A. Steen, and T.L. Schwarz. 2016. Phosphorylation-Induced Motor Shedding Is Required at Mitosis for Proper Distribution and Passive Inheritance of Mitochondria. *Cell Rep.* 16:2142–2155. doi:10.1016/J.CELREP.2016.07.055.

Cieri, D., M. Vicario, M. Giacomello, F. Vallese, R. Filadi, T. Wagner, T. Pozzan, P. Pizzo, L. Scorrano, M. Brini, and T. Calì. 2017. SPLICS: a split green fluorescent protein-based contact site sensor for narrow and wide heterotypic organelle juxtaposition. *Cell Death Differ.* 25: 1131-1145 doi:10.1038/s41418-017-0033-z.

Clift, D., W.A. McEwan, L.I. Labzin, V. Konieczny, B. Mogessie, L.C. James, and M.

Schuh. 2017. A Method for the Acute and Rapid Degradation of Endogenous Proteins. *Cell*. 171:1692-1706.e18. doi:10.1016/J.CELL.2017.10.033.

Dema, A., J. van Haren, and T. Wittmann. 2022. Optogenetic EB1 inactivation shortens metaphase spindles by disrupting cortical force-producing interactions with astral microtubules. *Curr. Biol.* 32:1197-1205.e4. doi:10.1016/J.CUB.2022.01.017.

Deubner, J., P. Coulon, and I. Diester. 2019. Optogenetic approaches to study the mammalian brain. *Curr. Opin. Struct. Biol.* 57:157–163. doi:10.1016/J.SBI.2019.04.003.

Eberhardt, E.L., A. V. Ludlam, Z. Tan, and M.A. Cianfrocco. 2020. Miro: A molecular switch at the center of mitochondrial regulation. *Protein Sci.* 29:1269–1284. doi:10.1002/PRO.3839.

Faville, R., B. Kottler, G.J. Goodhill, P.J. Shaw, and B. van Swinderen. 2015. How deeply does your mutant sleep? Probing arousal to better understand sleep defects in Drosophila. *Sci. Rep.* 5:8454. doi: 10.1038/srep08454

Fenton, A.R., T.A. Jongens, and E.L.F. Holzbaur. 2021. Mitochondrial adaptor TRAK2 activates and functionally links opposing kinesin and dynein motors. *Nat. Commun.* 12:4578. doi:10.1038/S41467-021-24862-7.

Floyd, C., H. Levine, C. Jarzynski, and G.A. Papoian. 2021. Understanding cytoskeletal avalanches using mechanical stability analysis. *Proc. Natl. Acad. Sci. U. S. A.* 118: e2110239118. doi:10.1073/PNAS.2110239118.

Fransson, Å., A. Ruusala, and P. Aspenström. 2006. The atypical Rho GTPases Miro-1 and Miro-2 have essential roles in mitochondrial trafficking. *Biochem. Biophys. Res. Commun.* 344:500–510. doi:10.1016/J.BBRC.2006.03.163.

Frederick, R.L., J.M. McCaffery, K.W. Cunningham, K. Okamoto, and J.M. Shaw. 2004. Yeast Miro GTPase, Gem1p, regulates mitochondrial morphology via a novel pathway. *J. Cell Biol.* 167:87–98. doi:10.1083/JCB.200405100.

Glater, E.E., L.J. Megeath, R.S. Stowers, and T.L. Schwarz. 2006. Axonal transport of mitochondria requires milton to recruit kinesin heavy chain and is light chain independent. *J. Cell Biol.* 173:545–557. doi:10.1083/JCB.200601067.

Guillén-Samander, A., M. Leonzino, M.G. Hanna, N. Tang, H. Shen, and P. De Camilli. 2021. VPS13D bridges the ER to mitochondria and peroxisomes via Miro. *J. Cell Biol.* 220: e202010004. doi:10.1083/JCB.202010004.

Guo, X., G.T. Macleod, A. Wellington, F. Hu, S. Panchumarthi, M. Schoenfield, L.

Marin, M.P. Charlton, H.L. Atwood, and K.E. Zinsmaier. 2005. The GTPase dMiro is required for axonal transport of mitochondria to Drosophila synapses. *Neuron*. 47:379–93. doi:10.1016/j.neuron.2005.06.027.

Gutnick, A., M.R. Banghart, E.R. West, and T.L. Schwarz. 2019. The light-sensitive dimerizer zapalog reveals distinct modes of immobilization for axonal mitochondria. *Nat. Cell Biol.* 21:768-777. doi:10.1038/s41556-019-0317-2.

Haberman, R.P., M.T. Koh, and M. Gallagher. 2017. Heightened cortical excitability in aged rodents with memory impairment. *Neurobiol. Aging*. 54:144–151. doi:10.1016/J.NEUROBIOLAGING.2016.12.021.

van Haren, J., L.S. Adachi, and T. Wittmann. 2020. Optogenetic Control of Microtubule Dynamics. *Methods Mol. Biol.* 2101:211–234. doi:10.1007/978-1-0716-0219-5_14.

Van Haren, J., R.A. Charafeddine, A. Ettinger, H. Wang, K.M. Hahn, and T. Wittmann. 2018. Local control of intracellular microtubule dynamics by EB1 photodissociation. *Nat. Cell Biol.* 20:252–261. doi:10.1038/S41556-017-0028-5.

Harterink, M., P. Van Bergeijk, C. Allier, B. De Haan, S. Van Den Heuvel, C.C. Hoogenraad, and L.C. Kapitein. 2016. Light-controlled intracellular transport in Caenorhabditis elegans. *Curr. Biol.* 26:R153–R154. doi:10.1016/J.CUB.2015.12.016.

Helle, S.C.J., Q. Feng, M.J. Aebersold, L. Hirt, R.R. Grüter, A. Vahid, A. Sirianni, S. Mostowy, J.G. Snedeker, A. Šarić, T. Idema, T. Zambelli, and B. Kornmann. 2017. Mechanical force induces mitochondrial fission. *Elife*. 6: e30292. doi:10.7554/ELIFE.30292.

Henrichs, V., L. Grycova, C. Barinka, Z. Nahacka, J. Neuzil, S. Diez, J. Rohlena, M. Braun, and Z. Lansky. 2020. Mitochondria-adaptor TRAK1 promotes kinesin-1 driven transport in crowded environments. *Nat. Commun.* 11:3123. doi:10.1038/S41467-020-16972-5.

Jolly, A.L., C.H. Luan, B.E. Dusel, S.F. Dunne, M. Winding, V.J. Dixit, C. Robins, J.L. Saluk, D.J. Logan, A.E. Carpenter, M. Sharma, D. Dean, A.R. Cohen, and V.I. Gelfand. 2016. A Genome-wide RNAi Screen for Microtubule Bundle Formation and Lysosome Motility Regulation in Drosophila S2 Cells. *Cell Rep.* 14:611–620. doi:10.1016/J.CELREP.2015.12.051.

Kang, J.-S., J.-H. Tian, P.-Y. Pan, P. Zald, C. Li, C. Deng, and Z.-H. Sheng. 2008. Docking of axonal mitochondria by syntaphilin controls their mobility and affects

short-term facilitation. *Cell*. 132:137–48. doi:10.1016/j.cell.2007.11.024.

König, T., H. Nolte, M.J. Aaltonen, T. Tatsuta, M. Krols, T. Stroh, T. Langer, and H.M. McBride. 2021. MIROs and DRP1 drive mitochondrial-derived vesicle biogenesis and promote quality control. *Nat. Cell Biol.* 23:1271–1286. doi:10.1038/s41556-021-00798-4.

Kottler, B., R. Faville, J.C. Bridi, and F. Hirth. 2019. Inverse Control of Turning Behavior by Dopamine D1 Receptor Signaling in Columnar and Ring Neurons of the Central Complex in Drosophila. *Curr. Biol.* 29:567-577.e6. doi:10.1016/J.CUB.2019.01.017.

Kwon, S.K., R. Sando, T.L. Lewis, Y. Hirabayashi, A. Maximov, and F. Polleux. 2016. LKB1 Regulates Mitochondria-Dependent Presynaptic Calcium Clearance and Neurotransmitter Release Properties at Excitatory Synapses along Cortical Axons. *PLOS Biol.* 14:e1002516. doi:10.1371/JOURNAL.PBIO.1002516.

Lee, K.-S., S. Huh, S. Lee, Z. Wu, A.-K. Kim, H.-Y. Kang, and B. Lu. 2018. Altered ER-mitochondria contact impacts mitochondria calcium homeostasis and contributes to neurodegeneration in vivo in disease models. *Proc. Natl. Acad. Sci. U. S. A.* 115:E8844–E8853. doi:10.1073/pnas.1721136115.

Lee, K.S., and B. Lu. 2014. The myriad roles of Miro in the nervous system: axonal transport of mitochondria and beyond. *Front. Cell. Neurosci.* 8:330. doi:10.3389/FNCEL.2014.00330.

Lee, S., K.S. Lee, S. Huh, S. Liu, D.Y. Lee, S.H. Hong, K. Yu, and B. Lu. 2016. Polo Kinase Phosphorylates Miro to Control ER-Mitochondria Contact Sites and Mitochondrial Ca(2+) Homeostasis in Neural Stem Cell Development. *Dev. Cell*. 37:174–189. doi:10.1016/J.DEVCEL.2016.03.023.

Li, L., D.M. Conradson, V. Bharat, M.J. Kim, C.H. Hsieh, P.S. Minhas, A.M. Papakyrikos, A.S. Durairaj, A. Ludlam, K.I. Andreasson, L. Partridge, M.A. Cianfrocco, and X. Wang. 2021. A mitochondrial membrane-bridging machinery mediates signal transduction of intramitochondrial oxidation. *Nat. Metab.* 3:1242–1258. doi:10.1038/S42255-021-00443-2.

Liu, S., T. Sawada, S. Lee, W. Yu, G. Silverio, P. Alapatt, I. Millan, A. Shen, W. Saxton, T. Kanao, R. Takahashi, N. Hattori, Y. Imai, and B. Lu. 2012. Parkinson's disease-associated kinase PINK1 regulates Miro protein level and axonal transport of mitochondria. *PLoS Genet.* 8: e1002537. doi:10.1371/JOURNAL.PGEN.1002537.

López-Doménech, G., C. Covill-Cooke, D. Ivankovic, E.F. Halff, D.F. Sheehan, R. Norkett, N. Birsa, and J.T. Kittler. 2018. Miro proteins coordinate microtubule- and actin-dependent mitochondrial transport and distribution. *EMBO J.* 37:321–336. doi:10.15252/EMBJ.201696380.

MacAskill, A.F., J.E. Rinholm, A.E. Twelvetrees, I.L. Arancibia-Carcamo, J. Muir, A. Fransson, P. Aspenstrom, D. Attwell, and J.T. Kittler. 2009. Miro1 Is a Calcium Sensor for Glutamate Receptor-Dependent Localization of Mitochondria at Synapses. *Neuron*. 61:541–555. doi:10.1016/j.neuron.2009.01.030.

Mahecic, D., L. Carlini, T. Kleele, A. Colom, A. Goujon, S. Matile, A. Roux, and S. Manley. 2021. Mitochondrial membrane tension governs fission. *Cell Rep.* 35: 108947. doi:10.1016/J.CELREP.2021.108947.

Modi, S., G. López-Doménech, E.F. Halff, C. Covill-Cooke, D. Ivankovic, D. Melandri, I.L. Arancibia-Cárcamo, J.J. Burden, A.R. Lowe, and J.T. Kittler. 2019. Miro clusters regulate ER-mitochondria contact sites and link cristae organization to the mitochondrial transport machinery. *Nat. Commun.* 10:4399. doi:10.1038/S41467-019-12382-4.

Murakoshi, H., M.E. Shin, P. Parra-Bueno, E.M. Szatmari, A.C.E. Shibata, and R. Yasuda. 2017. Kinetics of endogenous CaMKII required for synaptic plasticity revealed by optogenetic kinase inhibitor. *Neuron*. 94:37-47.e5. doi:10.1016/J.NEURON.2017.02.036.

Nemani, N., E. Carvalho, D. Tomar, Z. Dong, A. Ketschek, S.L. Breves, F. Jaña, A.M. Worth, J. Heffler, P. Palaniappan, A. Tripathi, R. Subbiah, M.F. Riitano, A. Seelam, T. Manfred, K. Itoh, S. Meng, H. Sesaki, W.J. Craigen, S. Rajan, S. Shanmughapriya, J. Caplan, B.L. Prosser, D.L. Gill, P.B. Stathopulos, G. Gallo, D.C. Chan, P. Mishra, and M. Madesh. 2018. MIRO-1 Determines Mitochondrial Shape Transition upon GPCR Activation and Ca2+ Stress. *Cell Rep.* 23:1005–1019. doi:10.1016/j.celrep.2018.03.098.

Nguyen, T.T., S.S. Oh, D. Weaver, A. Lewandowska, D. Maxfield, M.H. Schuler, N.K. Smith, J. Macfarlane, G. Saunders, C.A. Palmer, V. Debattisti, T. Koshiba, S. Pulst, E.L. Feldman, G. Hajnóczky, and J.M. Shaw. 2014. Loss of Miro1-directed mitochondrial movement results in a novel murine model for neuron disease. *Proc. Natl. Acad. Sci. U. S. A.* 111: E3631-40. doi:10.1073/PNAS.1402449111.

Niescier, R.F., K. Hong, D. Park, and K.T. Min. 2018. MCU Interacts with Miro1 to

Modulate Mitochondrial Functions in Neurons. *J. Neurosci.* 38:4666–4677. doi:10.1523/JNEUROSCI.0504-18.2018.

Oeding, S.J., K. Majstrowicz, X.P. Hu, V. Schwarz, A. Freitag, U. Honnert, P. Nikolaus, and M. Bähler. 2018. Identification of Miro1 and Miro2 as mitochondrial receptors for myosin XIX. *J. Cell Sci.* 131:jcs219469. doi:10.1242/JCS.219469.

Panchal, K., and A.K. Tiwari. 2020. Miro, a Rho GTPase genetically interacts with Alzheimer's disease-associated genes (Tau, Aβ 42 and Appl) in Drosophila melanogaster. *Biol. Open*. 9: bio049569. doi:10.1242/BIO.049569.

Qin, J., Y. Guo, B. Xue, P. Shi, Y. Chen, Q.P. Su, H. Hao, S. Zhao, C. Wu, L. Yu, D. Li, and Y. Sun. 2020. ER-mitochondria contacts promote mtDNA nucleoids active transportation via mitochondrial dynamic tubulation. *Nat. Commun.* 11:4471. doi:10.1038/S41467-020-18202-4.

Reis, K., Å. Fransson, and P. Aspenström. 2009. The Miro GTPases: At the heart of the mitochondrial transport machinery. *FEBS Lett.* 583:1391–1398. doi:10.1016/J.FEBSLET.2009.04.015.

Russo, G.J., K. Louie, A. Wellington, G.T. Macleod, F. Hu, S. Panchumarthi, and K.E. Zinsmaier. 2009. Drosophila Miro is required for both anterograde and retrograde axonal mitochondrial transport. *J. Neurosci.* 29:5443–55. doi:10.1523/JNEUROSCI.5417-08.2009.

Shaltouki, A., C.H. Hsieh, M.J. Kim, and X. Wang. 2018. Alpha-synuclein delays mitophagy and targeting Miro rescues neuron loss in Parkinson's models. *Acta Neuropathol.* 136:607–620. doi:10.1007/S00401-018-1873-4.

Simkin, D., S. Hattori, N. Ybarra, T.F. Musia, E.W. Buss, H. Richter, M. Matthew Oh, D.A. Nicholson, and J.F. Disterhoft. 2015. Aging-Related Hyperexcitability in CA3 Pyramidal Neurons Is Mediated by Enhanced A-Type K+ Channel Function and Expression. *J. Neurosci.* 35:13206. doi:10.1523/JNEUROSCI.0193-15.2015.

Song, Y., P. Huang, X. Liu, Z. Zhao, Y. Wang, B. Cui, and L. Duan. 2022. Light-inducible deformation of mitochondria in live cells. *Cell Chem. Biol.* 29:109-119.e3. doi:10.1016/J.CHEMBIOL.2021.05.015.

van Spronsen, M., M. Mikhaylova, J. Lipka, M.A. Schlager, D.J. van den Heuvel, M. Kuijpers, P.S. Wulf, N. Keijzer, J. Demmers, L.C. Kapitein, D. Jaarsma, H.C. Gerritsen, A. Akhmanova, and C.C. Hoogenraad. 2013. TRAK/Milton motor-

adaptor proteins steer mitochondrial trafficking to axons and dendrites. *Neuron*. 77:485–502. doi:10.1016/j.neuron.2012.11.027.

Stowers, R.S., L.J. Megeath, J. Górska-Andrzejak, I.A. Meinertzhagen, and T.L. Schwarz. 2002. Axonal transport of mitochondria to synapses depends on milton, a novel Drosophila protein. *Neuron*. 36:1063–77. doi: 10.1016/s0896-6273(02)01094-2.

Strickland, D., Y. Lin, E. Wagner, C.M. Hope, J. Zayner, C. Antoniou, T.R. Sosnick, E.L. Weiss, and M. Glotzer. 2012. TULIPs: Tunable, light-controlled interacting protein tags for cell biology. *Nat. Methods*. 9:379–384. doi:10.1038/nmeth.1904.

Vaccaro, V., M.J. Devine, N.F. Higgs, and J.T. Kittler. 2017. Miro1-dependent mitochondrial positioning drives the rescaling of presynaptic Ca^{2+} signals during homeostatic plasticity. *EMBO Rep.* 18:231–240. doi:10.15252/embr.201642710.

Vagnoni, A., and S.L. Bullock. 2016. A simple method for imaging axonal transport in aging neurons using the adult Drosophila wing. *Nat. Protoc.* 11:1711–1723. doi:10.1038/nprot.2016.112.

Vagnoni, A., and S.L. Bullock. 2018. A cAMP/PKA/Kinesin-1 Axis Promotes the Axonal Transport of Mitochondria in Aging Drosophila Neurons. *Curr. Biol.* 28:1265–1272. doi:10.1016/j.cub.2018.02.048.

Vagnoni, A., P.C. Hoffmann, and S.L. Bullock. 2016. Reducing Lissencephaly-1 levels augments mitochondrial transport and has a protective effect in adult Drosophila neurons. *J. Cell Sci.* 129:178–90. doi:10.1242/jcs.179184.

Wang, H., M. Vilela, A. Winkler, M. Tarnawski, I. Schlichting, H. Yumerefendi, B. Kuhlman, R. Liu, G. Danuser, and K.M. Hahn. 2016. LOVTRAP: an optogenetic system for photoinduced protein dissociation. *Nat. Methods*. 13:755–758. doi:10.1038/nmeth.3926.

Wang, X., and T.L. Schwarz. 2009. The Mechanism of Ca2+-Dependent Regulation of Kinesin-Mediated Mitochondrial Motility. *Cell*. 136:163–174. doi:10.1016/j.cell.2008.11.046.

Wong, C.O., N.E. Karagas, J. Jung, Q. Wang, M.A. Rousseau, Y. Chao, R. Insolera, P. Soppina, C.A. Collins, Y. Zhou, J.F. Hancock, M.X. Zhu, and K. Venkatachalam. 2021. Regulation of longevity by depolarization-induced activation of PLC-β-IP3R signaling in neurons. *Proc. Natl. Acad. Sci. U. S. A.* 118:e2004253118. doi:10.1073/PNAS.2004253118.

Yesbolatova, A., Y. Saito, N. Kitamoto, H. Makino-Itou, R. Ajima, R. Nakano, H.

Nakaoka, K. Fukui, K. Gamo, Y. Tominari, H. Takeuchi, Y. Saga, K. ichiro Hayashi, and M.T. Kanemaki. 2020. The auxin-inducible degron 2 technology provides sharp degradation control in yeast, mammalian cells, and mice. *Nat. Commun*. 11:1–13. doi:10.1038/s41467-020-19532-z.

Zhao, Y., E. Song, W. Wang, C.H. Hsieh, X. Wang, W. Feng, X. Wang, and K. Shen. 2021. Metaxins are core components of mitochondrial transport adaptor complexes. *Nat. Commun.* 12:83. doi:10.1038/S41467-020-20346-2.

Zullo, J.M., D. Drake, L. Aron, P. O'Hern, S.C. Dhamne, N. Davidsohn, C.A. Mao, W.H. Klein, A. Rotenberg, D.A. Bennett, G.M. Church, M.P. Colaiácovo, and B.A. Yankner. 2019. Regulation of lifespan by neural excitation and REST. *Nature.* 574:359–364. doi:10.1038/s41586-019-1647-8.

MATERIALS AND METHODS

Generation of plasmid DNA.

The new constructs produced in this study are reported in Supplementary Table 1 and were generated either through restriction enzymes mediated cloning or NEBuilder HiFi DNA Assembly (NEB) using the primers listed in Supplementary Table 2. The plasmid inserts were amplified by PCR using the Q5® Hot-Start High-Fidelity 2X Master Mix (NEB). Site-directed mutagenesis was performed using the Q5® Site-directed mutagenesis kit (NEB) following the manufacturer's instructions. The fidelity of all assembled constructs was verified by Sanger sequencing (Eurofins Genomics).

Isolation of Drosophila Miro cDNA.

Five Oregon-R flies were anesthetised on dry ice, rapidly grinded to powder with a plastic pestle in an Eppendorf tube and the total RNA extracted with the RNeasy Micro kit (Qiagen) following the manufacturer's instructions. Reverse transcription was performed with the iScript Select cDNA Synthesis kit (BioRad), using 1 µl of total RNA and Oligo dT primers. *Drosophila* Miro is encoded by a single gene, located on the third chromosome, from which potentially four different transcripts are produced (FlyBase reference: FBgn0039140). The coding sequence of the longest Miro-RE/Miro-RF isoform was amplified from the total *Drosophila* cDNA with the primer pair #1 and #2

(Supplementary Table 2) and was used as a template to engineer wild type Miro and the Split-Miro variants employed in this study.

Cell culture, transfection and RNAi.

Drosophila S2R+ cells were obtained from the Drosophila Genomics Research Centre (DGRC, Indiana University) and cultured in Schneider's insect medium (Gibco) at 25°C. Cells were transfected using FuGene HD transfection reagent (Promega) using a DNA:FuGene ratio of 1:3 following the manufacturer's instructions.

For RNAi experiments, 532 bp (Miro) and 599 bp (Control) dsRNA molecules were transcribed with the MEGAScript RNAi kit (Thermo Scientific) from templates generated by PCR of sequences within the Miro 3'-UTR (targeting only endogenous, and not overexpressed, Miro and Split-Miro) and the pT2-DsRed plasmid backbone, respectively. Primers used are listed in Supplementary Table 2. Cells were treated with 15 µg/ml dsRNA for a total of 6 days, replacing the dsRNA every 24 h in fresh media, prior to imaging.

***Drosophila* husbandry and generation of transgenic flies.**

The fly strains used in this study are listed in Supplementary Table 3. Flies were maintained on 'Iberian' food [70 mg/ml yeast (Brewer's yeast, MP Biomedicals, 903312), 55 mg/ml glucose (VWR, 10117HV), 7.7 mg/ml agar (SLS, FLY1020), 35 mg/ml organic plain white flour (Doves Farm, UK), 1.2 mg/ml Nipagin (Sigma, H3647), 0.4% propionic acid (Sigma-Aldrich, P5561] at 25°C and 60% humidity with a 12-h-light-12-h-dark cycle.

The transgenic fly lines generated in this study were obtained by phiC31-mediated transgenesis to integrate the relevant constructs into either the attP40 (25C6) or attP2 (68A4) landing sites following embryo injection.

Immunoprecipitation.

Cells were transfected in 10-cm dishes, washed with PBS and incubated with 900 µl IP lysis buffer (50 mM Trizma pH 7.4, 150 mM NaCl, 5 mM EDTA, 0.5% Triton X-100, 1x PhosSTOP^{TM}, 1x cOmplete EDTA-free protease inhibitor cocktail) on ice for 20 minutes. The cell lysate was homogenised through a 23G syringe needle and centrifuged at 21'000 g for 30 min at 4°C. 25 µl of GFP-Trap beads (Chromotek) were equilibrated by

washing 3x times in IP lysis buffer prior to the incubation with 1 mg of cleared lysate at 4°C overnight. After washing the beads 3x times with IP buffer, the immunoprecipitated material was eluted in 20 µl of 2X NuPAGE sample buffer supplemented with 40 mM DTT for 10 minutes at 95°C.

Western blotting.

Samples were loaded on a NuPAGE 4-12% Bis-Tris protein gel and transferred onto an Immobilion PVDF membrane (Merk-Millipore) for 1 h at 35 V in a wet transfer apparatus buffered with 12.5 mM Trizma-Base (Sigma), 96 mM glycine (Sigma), 10% methanol (Fisher Chemicals). The membrane was incubated in blocking solution [5% milk in PBST (PBS (pH 7.4) with 0.1% Tween-20 (VWR))] for 2 h and probed overnight with the following primary antibodies: anti-βtubulin (1:100, Developmental Studies Hybridoma Bank, DSHB #7, AB_2315513), anti-dMiro (Babic et al., 2015) (1:50000), anti-Milton (Stowers et al., 2002) (1:1000, monoclonal antibody 2A108), anti-GFP (1:1000, Chromotek, PABG1). Membranes were incubated for 1 h with either an IRDye secondary antibody (for LI-COR Odyssey imaging) or with horseradish peroxidase (HRP)-conjugated secondary antibodies followed by a 3-min incubation with a chemiluminescent substrate (GE Healthcare) for ChemiDoc imaging. Secondary HRP-conjugated antibodies: anti-rabbit (1:5000, NIF824), anti-mouse (1:5000, NIF825), anti-guinea pig (1: 5000, SeraCare 5220-0366). LI-COR secondary antibody: IR Dye 800CW goat anti-mouse IgG (1:10000).

Live cell imaging of cargo transport and photostimulation.

S2R+ cells were seeded in 4-well Nunc Lab-Tek chambered coverglass (Thermo Scientific) coated with 0.5 mg/ml Concanavalin A (Sigma). To induce the formation of cellular processes, cells were treated with 1 µM cytochalasin D (Sigma) for 3-4 h before imaging and throughout the imaging period. Before imaging, cells were stained with the following dyes, depending on the specific experimental setting: 200 nM MitoTracker Green FM, 200 nM MitoTracker DeepRed FM (Thermo Scientific), 100 nM MitoView 405 (Biotium), 1X TubulinTracker DeepRed (Thermo Scientific), 1X ActinTracker (CellMask Actin Tracker Stain, Invitrogen). The MitoView 405 dye was added to the cells 15 min prior imaging and kept throughout. All the other dyes were washed off prior to imaging, after 30 minutes of incubation. Live cell imaging was performed using a

Nikon A1RHD inverted confocal microscope, equipped with a photo-stimulation unit, GaAsP and multi-alkali PMT detectors, 405-nm, 488-nm, 561-nm and 640-nm laser lines and a Nikon 60X/1.4NA Plan Apochromatic oil immersion objective, unless specified otherwise. Experiments were carried out at a constant 25°C temperature in an Okolab incubation system and time series were digitally captured with the Nikon NIS-Elements software at 1 frame per seconds (fps), unless specified otherwise.

Sustained Split-Miro photocleavage in S2R+ cells was achieved with a 0.3% (0.017 mW) 488-nm laser, scan zoom of 4, at a framerate of 1 fps for the entire duration of the experiment. For dual colour imaging during sustained Split-Miro photocleavage, a frame every 1 min was acquired with either the 405-nm, 561 or 640-nm laser line. Transient whole-cell Split-Miro photocleavage was achieved with a stimulation step of 570 ms using a 4% 488-mn laser at a scan speed of 4 fps and 2 scanning iterations. In these experiments, a Nikon 40X/1.15NA Apochromatic water immersion objective with a scan zoom of 4 was used. The stimulation area was set to 492.7 μm^2, sufficient to cover the whole cell area. Time series before and after stimulation were acquired at 0.5 fps.

Imaging the neurons of the adult Drosophila wing was performed as reported in Vagnoni *et al.* (Vagnoni and Bullock, 2016, 2018). For rapid blue-light photostimulation in this tissue, a 5% (0.184 mW) 488-nm laser, scan zoom of 4, was used with a scan speed of 4 fps and 4 scanning iterations. The total duration of the stimulation step was 1.14 s and the stimulation area was set to cover a 46.23 μm^2 region of the neuronal axons.

Analysis of mitochondrial transport and morphology.

Mitochondrial motility in S2R+ cells was quantified in 2 – 6 processes for each cell. Only processes which remained in the same focal plane throughout acquisition and had no or minimal crossing with other processes, were selected. Each process was straightened using the 'Straighten' function in Fiji/ImageJ and kymographs produced and analysed with the 'Velocity Measurement Tool' (https://dev.mri.cnrs.fr/projects/imagej-macros/wiki/Velocity_Measurement_Tool) in Fiji/ImageJ.

'Run' was defined as a continuous movement which lasts for at least 3 seconds without any change in direction or velocity. Mitochondria were defined as 'motile' if engaging in at least one run ≥ 2 µm. A 'pause' was defined as a period of at least 3 seconds during which the mitochondrion does not change its position. The duty cycle describes the

motile behaviour of the mitochondria as percentage of time spent on long runs (≥ 2 µm), short runs (< 2 µm) and pausing, or in the anterograde and retrograde direction.

Mitochondrial morphology in the cell soma was analysed from cells showing a clearly interconnected network before photocleavage, using Fiji/ImageJ and a pipeline adapted from Chaudhry *et al.* (Chaudhry et al., 2020). Briefly, the 'Adaptive Threshold' command was used to create binary images which were individually checked for accuracy in marking the mitochondrial network. The 'Analyse particles' command was used to measure mitochondrial size, with a cut-off set at 0.09 μm^2. A skeleton of the mitochondrial network within each cell was obtained and analysed with the 'Skeletonize' and 'Analyze skeleton (2D/3D)' functions, respectively. Mitochondrial mass was defined as the total area covered by mitochondria within the cell and normalised to the first time point. The mitochondrial aspect ratio (AR) was measured in single mitochondria smaller than 6 μm^2 and was defined as the ratio between the longest and the shortest axis of the organelle. For the analysis of the mitochondrial network branching, only branches emanating from the main mitochondrial skeleton were considered.

Analysis of Split-Miro kinetics.

The kinetics of the cytoplasmic release of mCherry-tagged Split-Miro N-terminus after photocleavage and the reconstitution at the mitochondria was analysed by measuring the cytosolic fluorescence intensity of the mCherry before and after photocleavage. For cell culture experiments, images were analysed with the General Analysis tool of the Nikon NIS-Elements Software by defining an ROI covering the cellular cytosol (with no mitochondria) and measuring the fluorescence intensity at each time point. For neuronal *in vivo* experiments, images were analysed with Fiji/ImageJ by measuring the fluorescence intensity of a 0.126-μm^2 cytosolic ROI devoid of mitochondria. For each cell or fly wing, the fluorescence intensity over time was normalised to a scale from 0 to 1, where 0 corresponds to the minimum value measured before Split-Miro N-terminus release and 1 to the maximum value measured after photocleavage.

Live cell calcium imaging.

S2R+ cells were imaged with a Nikon Ti-E inverted epifluorescence microscope equipped with a Nikon 60X/1.4NA Plan Apochromatic oil immersion objective, a mercury lamp (Nikon Intensilight C-HGFI) for illumination and a Dual Andor Neo sCMOS camera for detection. Cells were plated on a Concanavalin A-coated 18-mm

coverslip and imaged in a Ludin imaging chamber (Type 1, Life Imaging Services) in S2 media. Cells were imaged at 1 fps for 3 minutes under blue-light which was sufficient to induce Split-Miro-dependent mitochondrial network retraction, prior to ionomycin stimulation. A peristaltic pump system (Ismatec) was used to perfuse the imaging chamber with 2.5 μM ionomycin (ThermoFischer Scientific) until all the media in the chamber was replaced. Additional 5-minutes imaging at 1 fps was performed to record the dynamic mito-GCaMP6 signal. To verify Split-Miro cleavage, a frame with green light (to capture mCherry-Split-MiroN) was acquired at the beginning and the end of each acquisition period.

To quantify mitochondrial calcium, a region of interest (ROI) was drawn to outline single cells and the fluorescence intensity of mito-GCaMP6f signal measured using the Nikon NIS-Elements software. Response curves were aligned at the base of the response peak and, for each cell, the fluorescence intensity at every time point was normalised to the value of the first frame. Only cells that responded at least 2-fold to ionomycin in the first 100 s were included in the quantification. mito-GCaMP6f 'peak' was defined as the maximum fold-change value reached during imaging. The time to reach the peak was calculated as the Δt between the 'peak' timepoint and the time of first response to stimulation.

Behavioural assay.

Flies were anesthetised with CO_2 on the day of eclosion, transferred to new food and aged for either 2 or 8 days prior to the assay. On the day of the assay, flies were briefly anesthetised on ice and individually loaded into 65-mm glass-tubes on custom-made platforms. Fly activity was recorded in an optogenetic enclosure (BFK Lab Ltd) equipped with LEDs for 444-nm blue light stimulation and a webcam for video recording. The position of each fly was automatically tracked and the quantification of the fly locomotor activity performed using the *Drosophila* ARousal Tracking (DART) system (Faville et al., 2015; Kottler et al., 2019). Flies were left to acclimatise for 20 min before starting the experiment. Fly activity was recorded continuously for 30 minutes before the blue LED light was switched on for 2 hours (power at the platform: 5 mW/cm^2). After the blue light was switched off, fly movements were recorded for an additional hour, for a combined experimental time of 3 hours, 30 minutes. Flies were defined as 'active' if displaying bouts of activity of at least 2 mm/s. The active average speed refers to the

speed of fly movement when active. The action initiation is defined as the number of times a bout of activity is started per second. The % activity represents the percentage of time the fly spends moving.

Statistical analysis and image preparation.

Data were analysed with Microsoft Excel and GraphPad Prism 9. Statistical tests and number of replicates are reported in the figure legends. Images were assembled using Fiji/ImageJ. For presentation purposes, ‘Subtract Background’ (rolling ball radius = 20 pixels), and either the ‘Despeckle’ or ‘Smooth’ filters were used to reduce salt and pepper noise. All images in the same experimental series were processed in the same manner.

FIGURE LEGENDS

Figure 1. Split-Miro is a photocleavable version of *Drosophila* Miro. A) Schematic of Split-Miro functional domains. **B)** Schematic representation of reconstituted and photocleaved mitochondrial-bound Split-Miro in its dark and lit state, respectively. Split-MiroN and Split-MiroC moieties can be followed independently by tagging them with different combinations of fluorescent proteins (e.g., EGFP/mCherry). **C)** Split-Miro is reconstituted and localises at the mitochondria in the absence of sustained blue-light irradiation. S2R+ cells were co-transfected with mCherry-tagged Split-MiroC (magenta) and EGFP-tagged Split-MiroN (green), mitochondria are stained with MitoTracker Deep Red (MTDR, cyan). **D)** Localisation of Split-Miro in S2R+ cells transfected with mCherry-Split-MiroN harbouring the T406A, T407A mutations in the N-terminus of LOV2 (Van Haren et al., 2018; Strickland et al., 2012) and untagged Split-MiroC, before and after a 570-ms pulse of blue light. Before irradiation, Split-Miro is reconstituted at the mitochondria, indicated by the warmer colour heatmap. mCherry-Split-MiroN is fully released into the cytoplasm (indicated by a more homogenous magenta colour) immediately after irradiation (8 s), and it fully reconstitutes within 120 s. Cartoon depicts photocleavage and reconstitution of mCherry-Split-Miro at different time points. s, seconds. **E-F)** Quantification of mCherry-Split-MiroN half-time release (E) and recovery (F) after photocleavage, relative to D. In (F), left panel shows levels of cytosolic Split-Miro N-terminus quantified after the maximum release is reached; right panel: recovery half-time. Data are shown as mean ± SEM. Solid line in (F) is exponential curve fit. Circles, number of cells, from two independent experiments. Scale bars: 10 µm.

Figure 2. Miro regulates mitochondrial motility in the processes of S2R+ cells and Split-Miro photocleavage reverts the effect of Split-Miro overexpression on mitochondrial motility but not velocity. A) Example of S2R+ cell treated with cytochalasin D to induce the formation of microtubule-rich processes. The microtubules and the mitochondria are stained with Tubulin Tracker and with MitoTracker Green (MitoTracker), respectively. White arrows indicate examples of cellular processes containing mitochondria. Scale bar: 10 µm. **B)** Representative kymographs of mitochondrial transport in the cellular processes of S2R+ cells treated with control (upper panel) or Miro dsRNA (bottom panel). Yellow highlights indicate examples of short (< 2 µm) and long runs (≥ 2 µm). Scale bars: 1 µm (distance) and 5 s (time). **C)**

Duty cycle analysis describes the average time mitochondria spend on long runs, short runs or pausing. For each parameter, all mitochondrial values from each cell were averaged and compared between control and Miro dsRNA condition. **D)** Percentage of motile mitochondria in cellular processes. Number of mitochondria analysed are in brackets, from 29 (Ctrl dsRNA) and 36 (Miro dsRNA) cells, from two independent experiments. Data are shown as mean ± SEM, multiple Student's t-tests (C) and Mann-Whitney test (D). This analysis suggests Miro is necessary to drive mitochondrial motility in *Drosophila* S2R+ cells and this is mainly due to modulation of long-range transport, while short-range motility appears to be largely independent of Miro. **E)** Representative kymographs showing mitochondrial transport in S2R+ cellular processes before and during exposure to blue light. Control cells were co-transfected with mCherry-tagged wt-Miro, which cannot be photocleaved, and EGFP targeted to the mitochondria via the Zdk1-MiroC anchor (EGFP-mito). Split-Miro was tagged with both -EGFP and mCherry to independently follow the C-terminal and N-terminal half, respectively. Mitochondrial transport was first imaged with a 561-nm laser, to capture the mCherry signal, and then with a 488-nm laser, to capture the EGFP signal while photocleaving Split-Miro (Movie 3). Cartoon depicts schematic of the transfected constructs. Scale bars: 5 µm (distance) and 30 s (time). **F)** Duty cycles analysis and **G)** percentage of motile mitochondria in cellular processes. In F-G, mitochondrial transport was first analysed following the mCherry tag in cells expressing either mCherry-tagged wt-Miro or Split-Miro (561-nm laser). In a separate experiment (488-nm laser), mitochondrial transport was quantified following the EGFP tag at the beginning (1st minute) and at the end (7th minute) of the time-lapse imaging with 488-nm blue light, as shown in panel E. In F, for each parameter, all mitochondrial values from each cell were averaged and compared to the control condition (561-nm laser) or to the first minute of blue light exposure (488-nm laser). Data are shown as mean ± SEM, from three independent experiments. Statistical significance was evaluated by one-way ANOVA followed by Tukey's post-hoc test (561-nm laser) or multiple paired t-tests (488-nm laser) in (F) and by Kruskal-Wallis test followed by Dunn's post-hoc test (561-nm laser) or by Mann-Whitney test (488-nm laser) in (G). Number of mitochondria analysed are in brackets, from 16 (Control), 15 (wt-Miro) and 15 (Split-Miro) cells under 561-nm laser, and 11 (wt-Miro) and 17 (Split-Miro) cells under 488-nm laser. **H)** Distribution of anterograde and retrograde long run velocity after wt-Miro and Split-Miro overexpression (561-nm laser) and after irradiation with blue light to photocleave Split-

Miro (488-nm laser). Solid lines are fitted curves. Statistical significance was calculated with a Kruskal-Wallis test followed by Dunn's post-hoc test (561-nm laser) and a Mann-Whitney test (488-nm laser). N = number of mitochondrial runs. * $p < 0.05$, ** $p < 0.01$, *** $p < 0.001$.

Figure 3. Split-Miro-dependent changes of mitochondrial morphology and connectivity are rescued by SNPH expression. A) Representative images of mitochondria in *Drosophila* S2R+ cells at the beginning (0 min) and after 3 and 7 minutes of exposure to blue light, which leads to Split-Miro, but not wt-Miro, photocleavage. Control cells (top panels) were co-transfected with mCherry-tagged wt-Miro (magenta) and EGFP targeted to the mitochondria via the Zdk1-MiroC anchor (EGFP-mito, grey). Split-Miro (bottom panels) was tagged with both EGFP and mCherry to independently follow the C-terminal and N-terminal half, respectively. The mCherry is shown at the beginning and end of the imaging period to confirm retention on and release from the mitochondria in wt-Miro and Split-Miro transfected cells, respectively, under blue light. Scale bar: 10µm. **B)** Quantification of mitochondrial aspect ratio (AR) and **C)** of the number of mitochondrial branches within the network, relative to A. **D)** Quantifications of the mitochondrial collapse phenotype after 7 minutes of time-lapse imaging with 488-nm blue light in S2R+ cells overexpressing wt-Miro and Split-Miro with or without a Miro dsRNA construct ($Miro^{RNAi}$). Number of cells: wt-Miro = 15, Split-Miro = 15, Split-Miro + $Miro^{RNAi}$ = 10, Fisher's exact test. **E)** Representative images of cells expressing mCherry-Split-Miro (Split-Miro, yellow) with either an empty vector (top panels) or with EGFP-SNPH (SNPH, bottom panels, grey) and stained with MitoTracker DeepRed (MTDR, magenta). White arrows show examples of mitochondria that have retracted after Split-Miro photocleavage. Diffuse cytoplasmic yellow signal indicates release of Split-Miro N-terminus from the mitochondria. Scale bar: 10 µm. **E')** Magnified inset shows examples of stable SNPH-positive mitochondria (white arrowheads) and dynamic mitochondrial membranes devoid of SNPH (magenta arrowheads). Scale bar: 2 µm. Not shown, Split-Miro. **F)** Quantification of mitochondrial AR and **G)** number of mitochondrial branches at the time points indicated, relative to E. Circles represent the average AR calculated from single mitochondria within the same cell (B, F) and the average number of branches per cell normalised to the average group value (Split-Miro, Split-Miro + SNPH) at timepoint 0 (C, G). Comparison across timepoints was performed by repeated-measures one-way ANOVA followed by Tukey's post-hoc test (B-C, F) and

Friedman test followed by Dunn's post-hoc test (G), from three independent experiments. Data are reported as mean ± SEM. * $p < 0.05$, ** $p < 0.01$, **** $p < 0.0001$.

Figure 4. Split-Miro photocleavage does not affect $[Ca^{2+}]_m$ abundance. A) Representative image of an S2R+ cell showing mitochondrial targeting of mito-GCaMP6f (cyan) in the perinuclear region (white arrows) and in single mitochondria (arrowheads). Yellow is mCherry-tagged wt-Miro (wt-Miro), magenta is MitoTracker DeepRed (MTDR). Scale bar: 5 µm. **B)** Cells transfected with mito-GCaMP6f and either mCherry-wt-Miro (wt-Miro) or mCherry-Split-Miro (Split-Miro) were stained with MTDR and the ratio of mito-GCaMP6f/MTDR signal intensity was analysed at the beginning (1st minute) and at the end (7th minute) of the time-lapse imaging under blue light. Number of cells: wt-Miro = 12, Split-Miro = 16; from three independent experiments. Data are shown as mean ± SEM. Repeated measures one-way ANOVA followed by Tukey's post-hoc test did not show any significant difference between groups, indicating the basal $[Ca^{2+}]_m$ does not significantly change after Split-Miro photocleavage. **C)** Expression of mCherry-Split-Miro (Split-Miro) or EBFP-SNPH (SNPH) does not significantly alter $[Ca^{2+}]_m$ uptake in cells challenged with ionomycin, compared to control conditions. Traces indicate the average mito-GCaMP6f fluorescence intensity values (circles) at individual time point before and after cell exposure to ionomycin (arrow). N = number of cells, from five independent experiments. **D-E)** Normalised response peak and time to reach the peak, respectively, relative to the data shown in C. Circles, number of cells. Kruskal-Wallis test followed by Dunn's multiple comparisons showed no difference between conditions.

Figure 5. Optogenetic control of *Drosophila* locomotor behaviour in Split-Miro flies. A) Adult *miro*$^{Sd32/B682}$ flies eclosed after *Appl-Gal4*-driven expression of UAS-wt-Miro, UAS-Split-Miro or UAS-Split-Miro + UAS-EGFP-SNPH (UAS-SNPH) were counted from 6, 5, and 3 independent crosses, respectively. Data are reported as percentage of flies expected from mendelian ratios. Data are mean ± SEM, one-way ANOVA with Tukey's post-hoc test showed no statistical difference. **B)** Schematic of the 'Opto-DART' behavioural setup consisting of a custom-made optogenetic enclosure equipped with LEDs for blue light stimulation and a camera to record fly activity. Flies are transferred to a 1D platform for automated recording of activity using the DART system(Faville et al., 2015; Kottler et al., 2019). DAC: Digital-to-Analog Converter for multi-platform integration. **C-H)** Overall activity, action initiation, and average speed of 2-day old flies

(C-E) and 8-day old flies (F-H) expressing UAS-wt-Miro or UAS-Split-Miro, before, during and after blue light exposure (shaded blue rectangles). In C and F, the average activity of flies expressing UAS-wt-Miro vs UAS-Split-Miro is: *before light exposure*, 3.78% ± 0.94 vs 2.34% ± 0.72 (p = 0.11)(C) and 5.62% ± 1.02 vs 8.7% ±1.81 (p = 0.14)(F); *under blue light*, 9.52% ± 0.96 vs 7.32% ± 0.81 (p = 0.13)(C) and 8.45% ± 0.82 vs 21.87% ± 2.07**** (F); *after blue light exposure*, 3.36% ± 1.18 vs 7.85% ± 1.96 (p = 0.13)(C) and 3.23% ± 1.1 vs 13.19% ± 2.39** (F). **I-K)** Overall activity, action initiation, and average speed of 8-day old flies expressing UAS-Split-Miro or UAS-Split-Miro + UAS-SNPH, before, during and after blue light exposure (shaded blue rectangles). In I, the overall activity of flies expressing UAS-Split-Miro vs UAS-Split-Miro + UAS-SNPH is: 6.09% ± 0.89 vs 0.95% ± 0.35**** before light exposure; 18.62% ± 1.4 vs 3.55% ± 0.75**** under blue light; 9.9% ± 1.4 vs 3.91% ± 1.25* after blue light exposure. In C-K, n = number of flies. Values are means ± SEM, Mann-Whitney test with Holm-Sidak test for multiple comparisons. * $p < 0.05$, ** $p < 0.01$, *** $p < 0.001$, **** $p<0.0001$.

Figure 6. Model for Split-Miro-mediated regulation of mitochondrial motility. The Split-Miro trafficking data are consistent with a model in which two different pools of mitochondria co-exist in S2R+ cells. After overexpression, Split-Miro recruits the motor complexes on the mitochondria and activates transport. On one mitochondrial pool (*mitochondrial pool 1*), Split-Miro links directly or indirectly (for example, via Milton/Trak, not depicted) to the motor proteins. On another subset of mitochondria (*mitochondrial pool 2*), the motor complexes are instead stabilised on the organelle by an unknown factor (question mark) following Miro-dependent recruitment. After Split-Miro photocleavage, *mitochondrial pool 1* can reverse to control levels of processivity or become stationary (Fig. 2F-G). However, the processivity (e.g., velocity and run length) of the *mitochondrial pool 2* is not affected as the recruited motors are not directly linked to the mitochondria via Miro (Fig. 2H, Supplementary Fig. 2J-K). Not depicted, dynein motor complex.

Split-Miro-dependent recruitment of motor complexes on an interconnected mitochondrial network, such as the one found in the perinuclear area of the cell soma, could cause significant tension on the network. Releasing the Split-Miro anchor by photocleavage, even if only on a subset of the mitochondria, would be sufficient to release the tension and cause mitochondrial network retraction, as shown in Fig. 3.

Figure 1

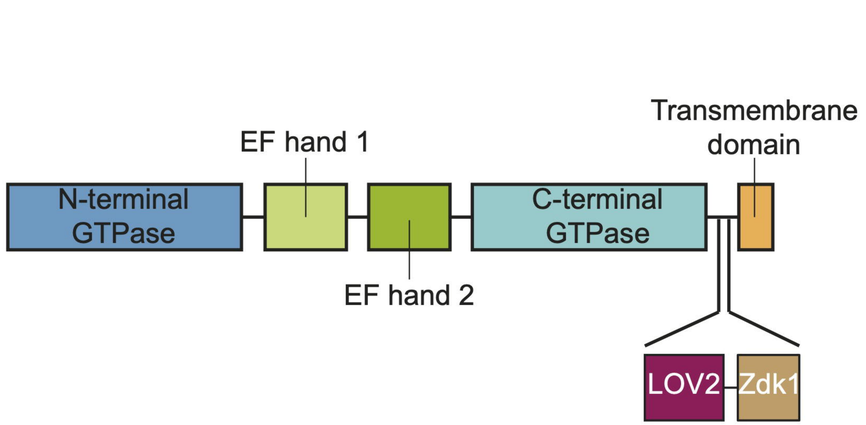

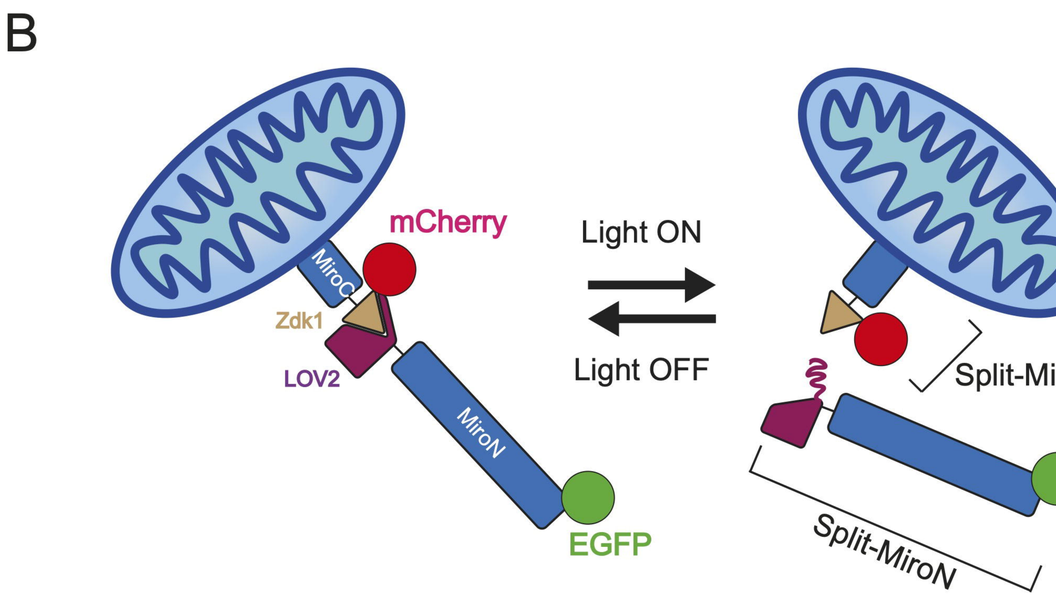

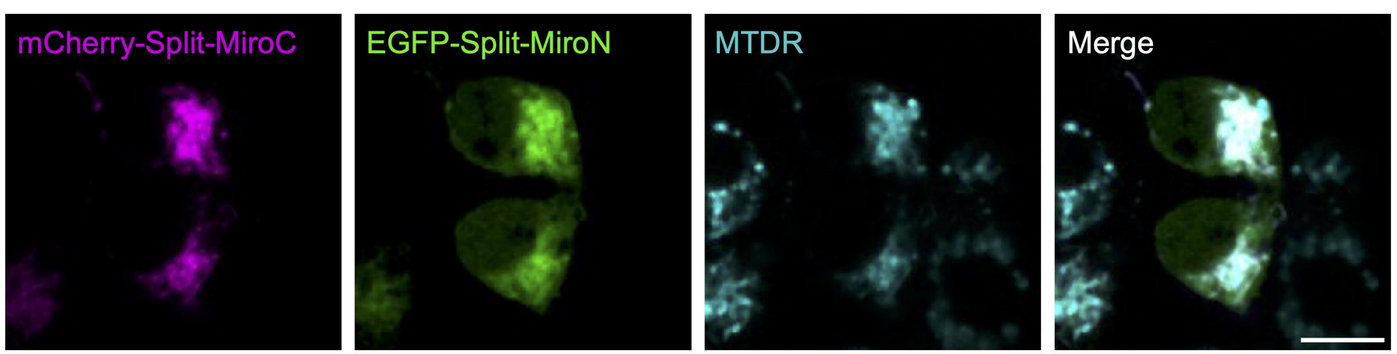

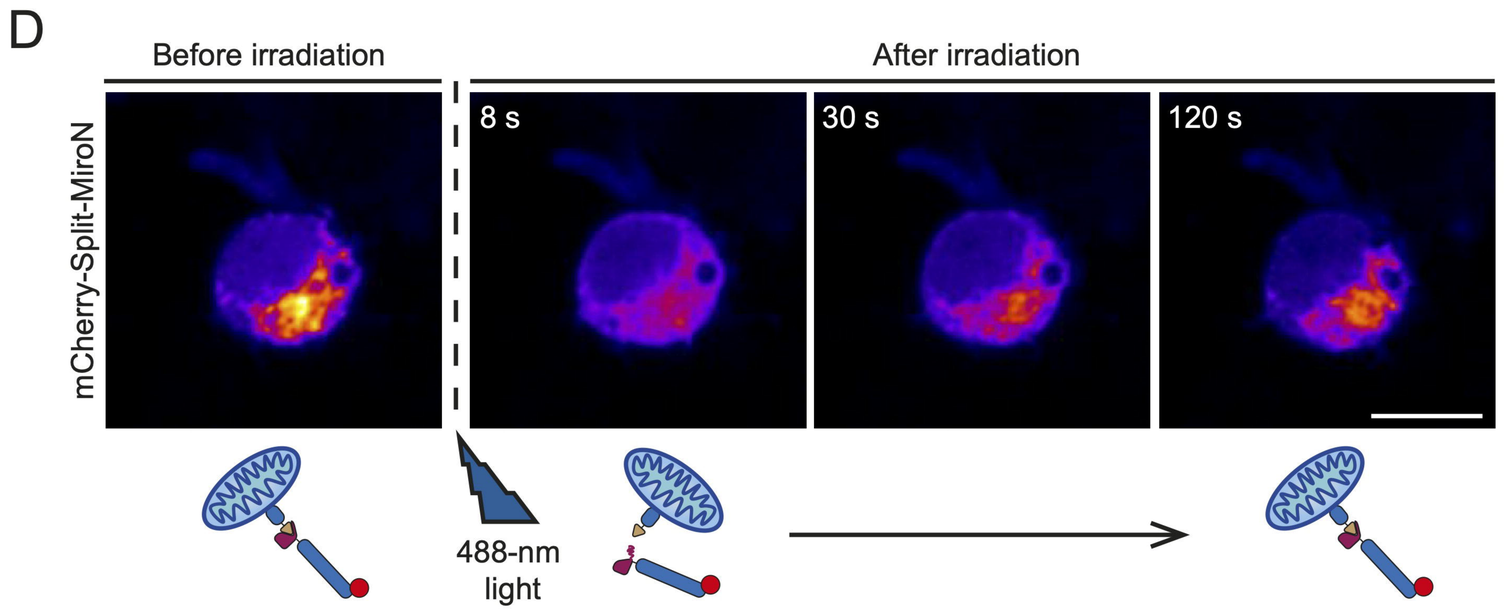

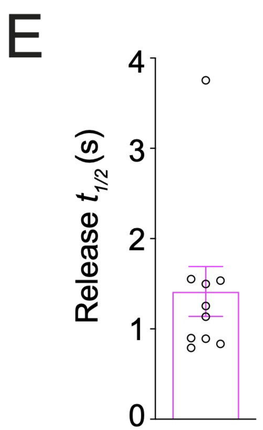

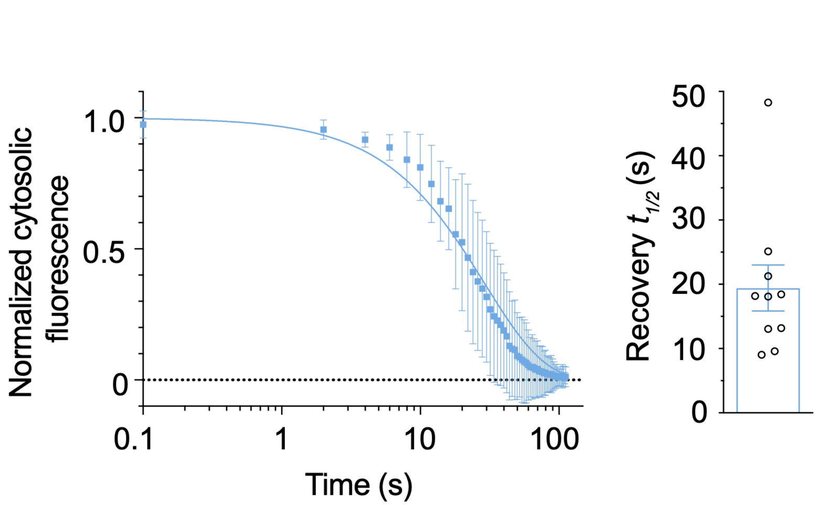

Figure 2

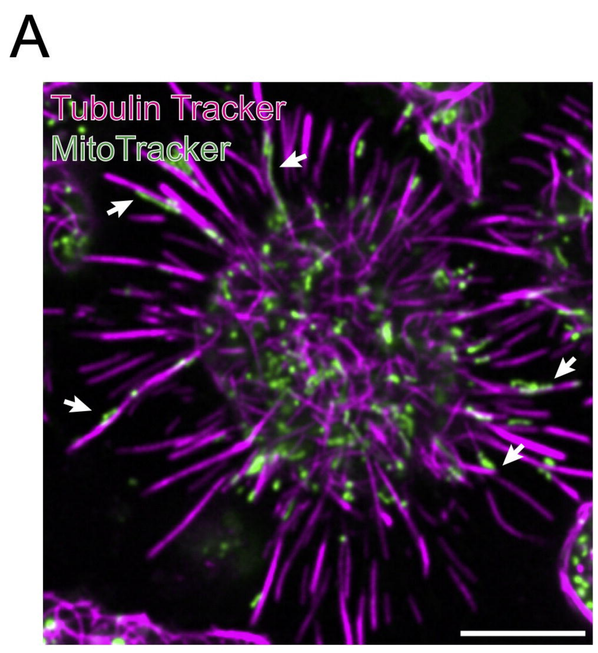

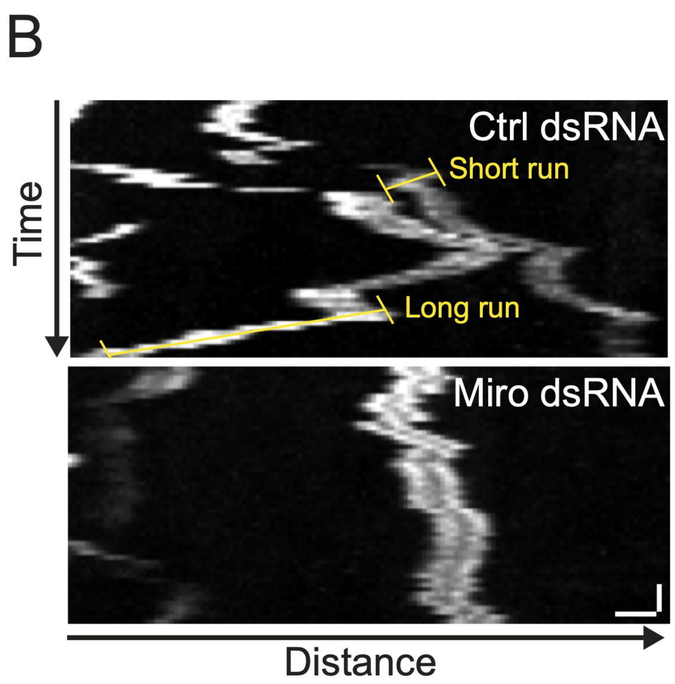

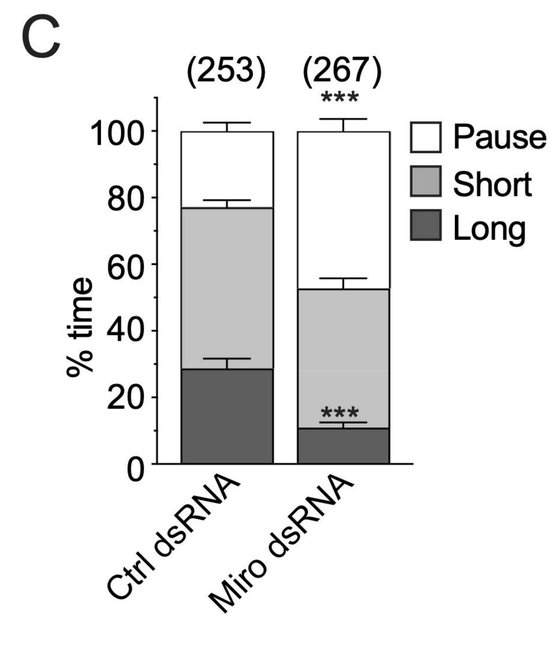

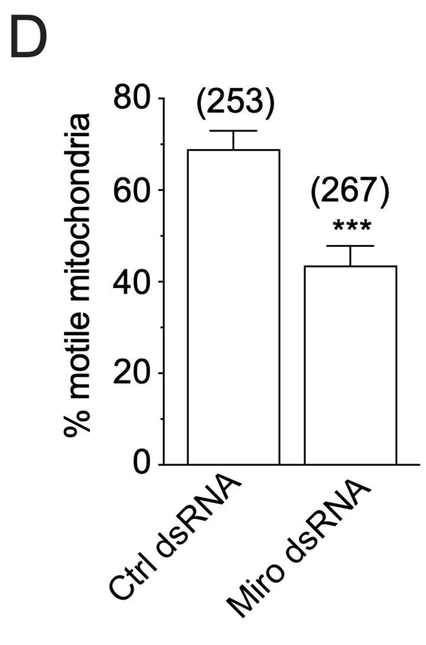

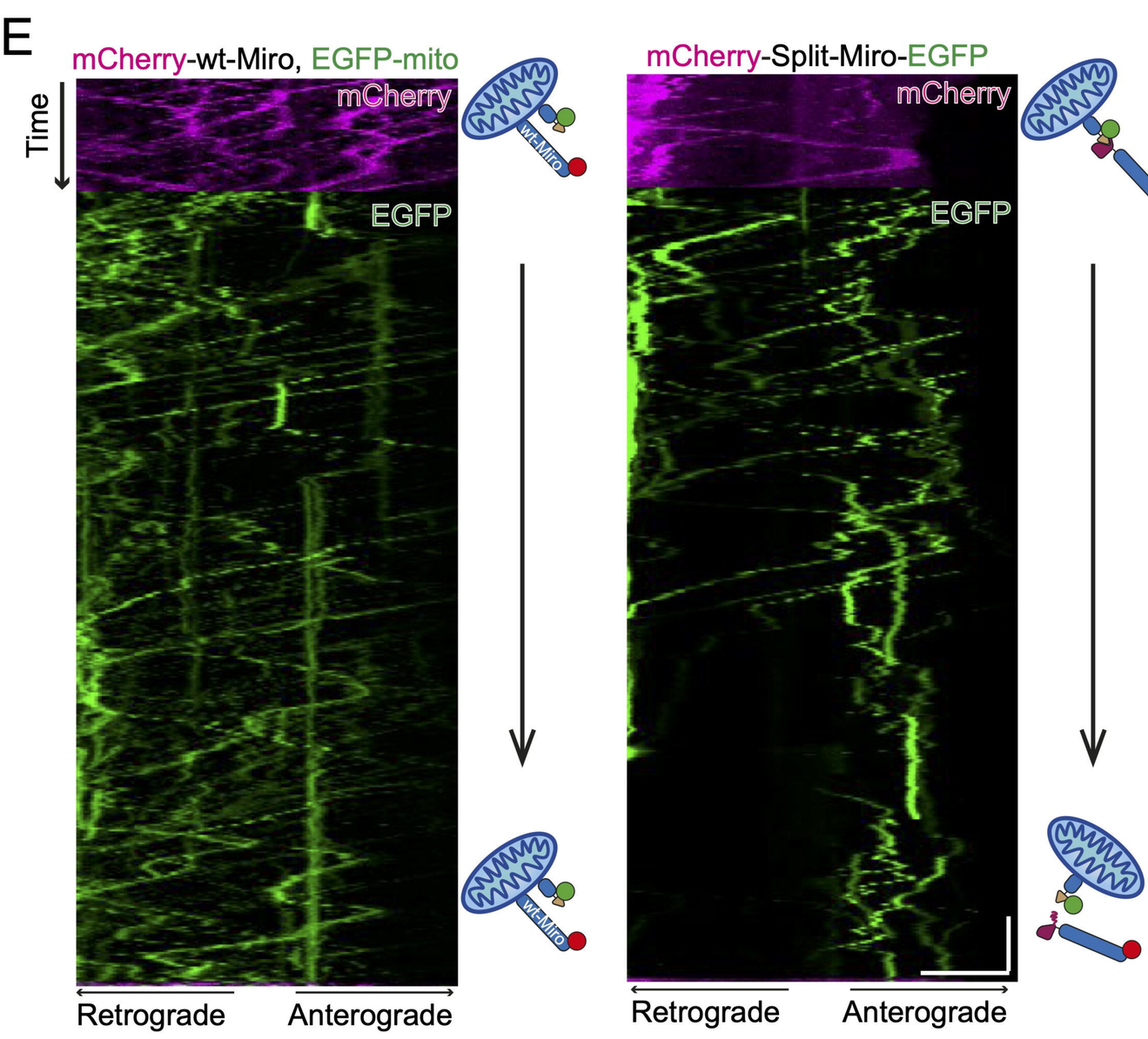

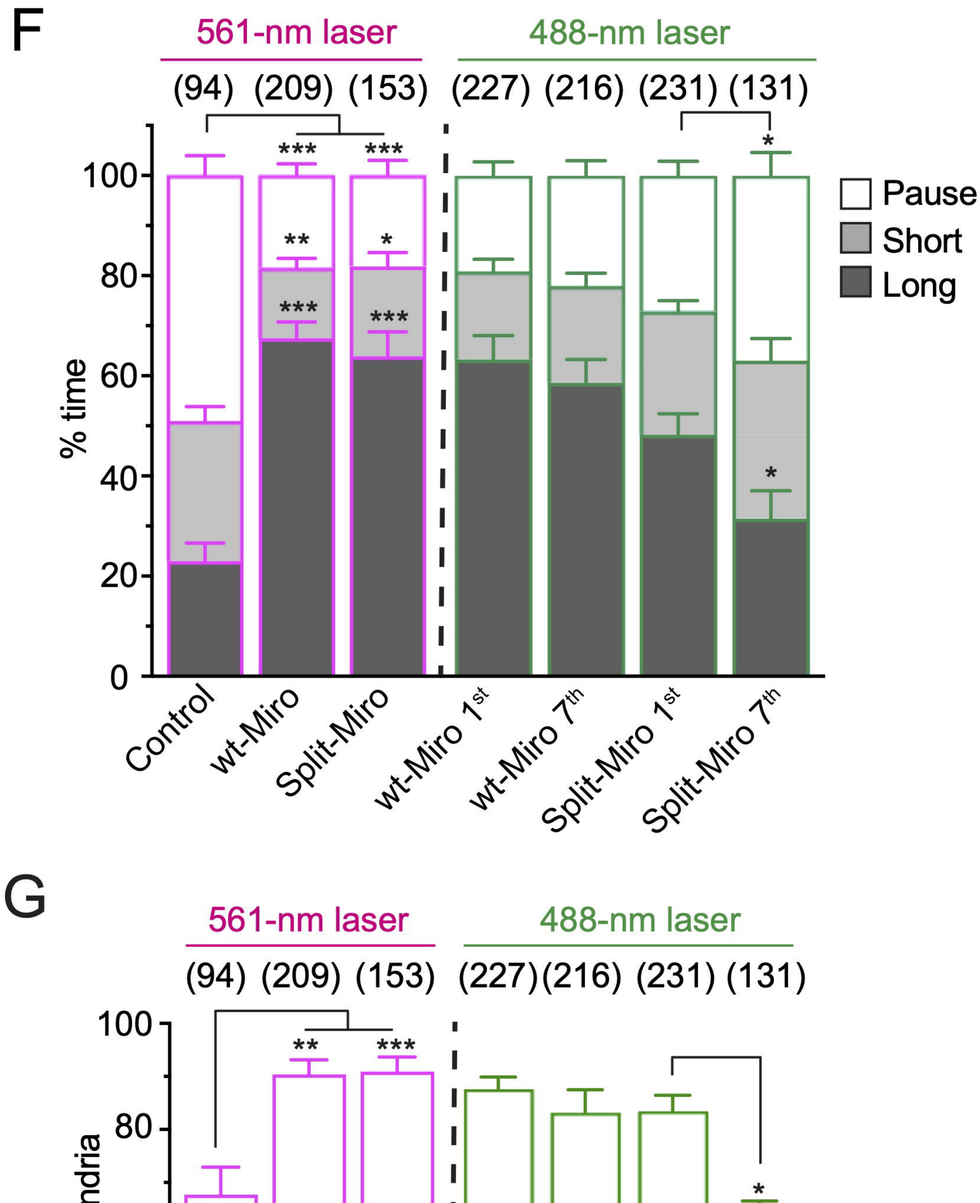

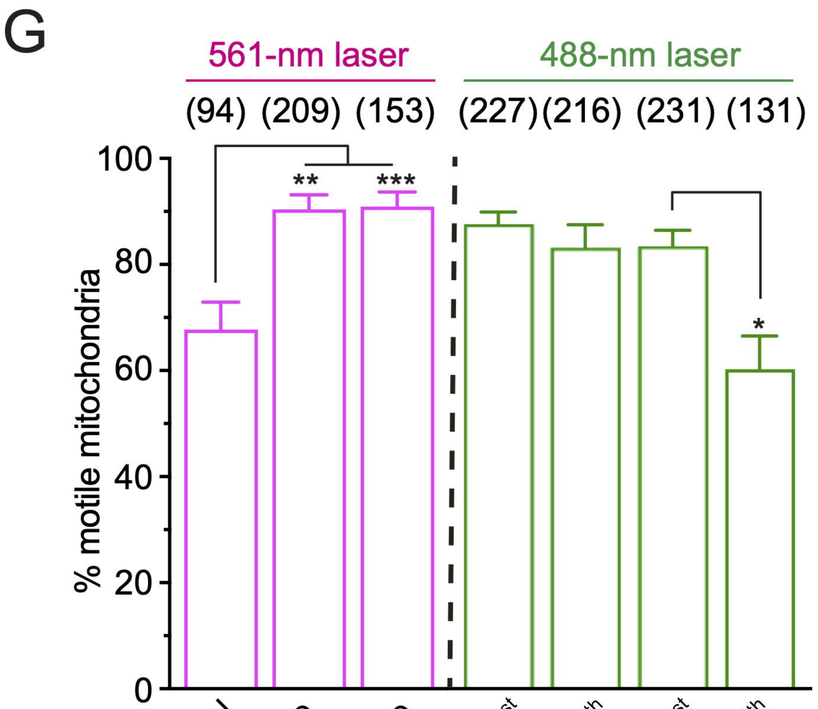

Figure 3

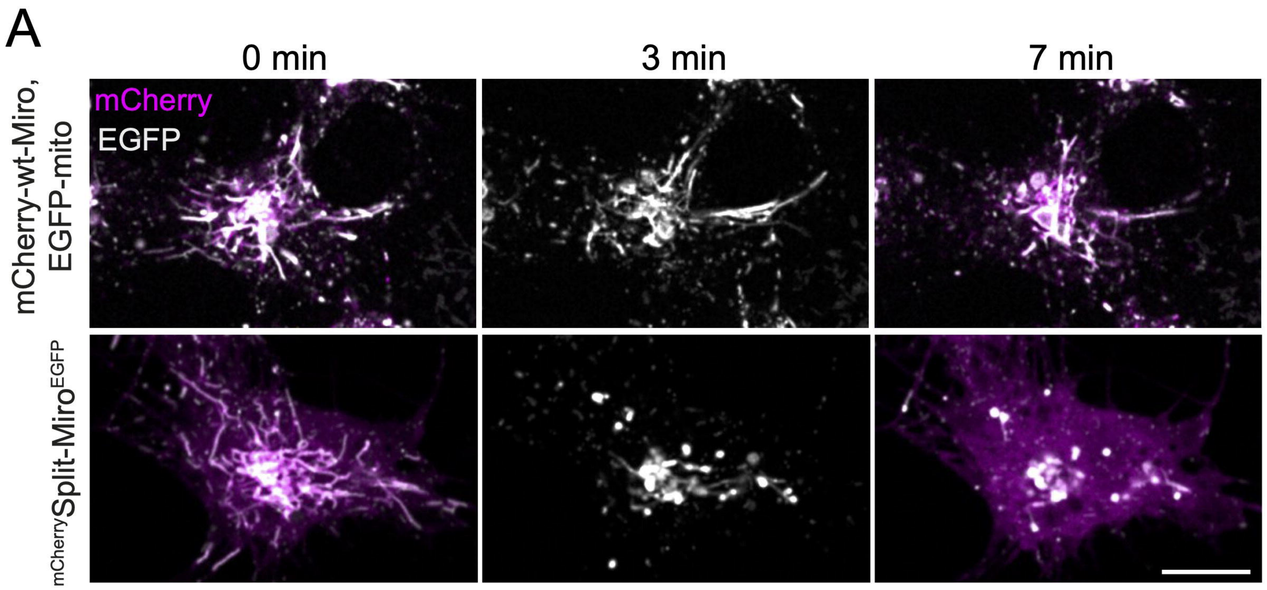

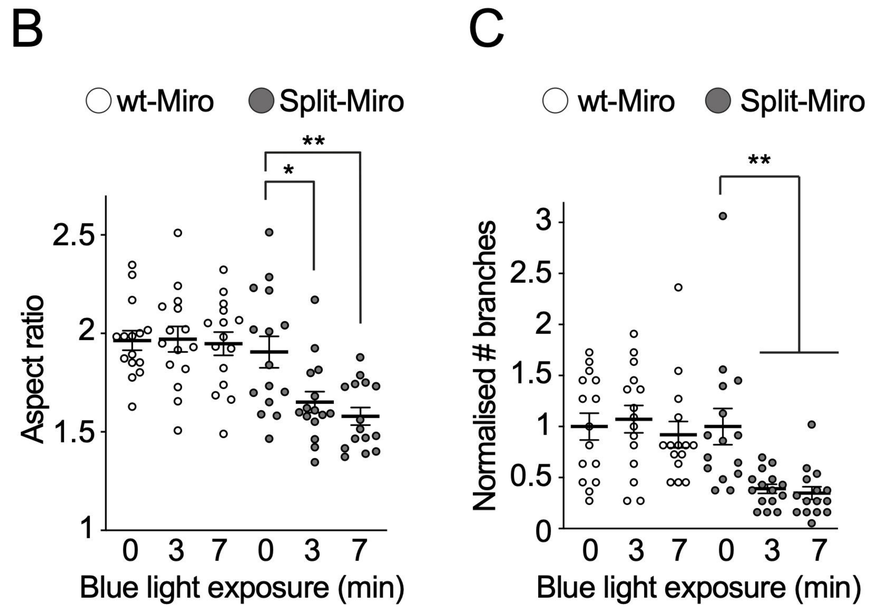

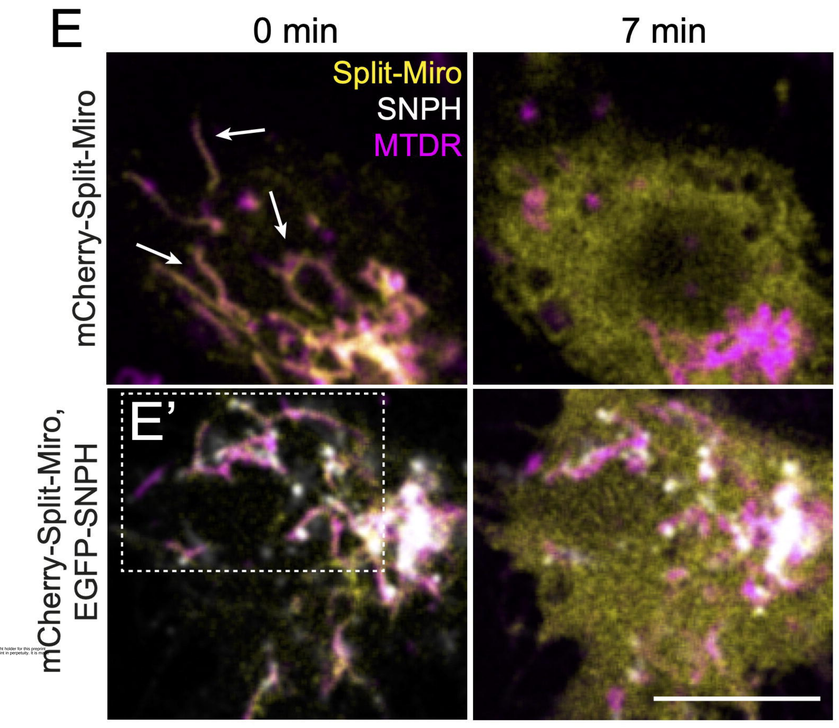

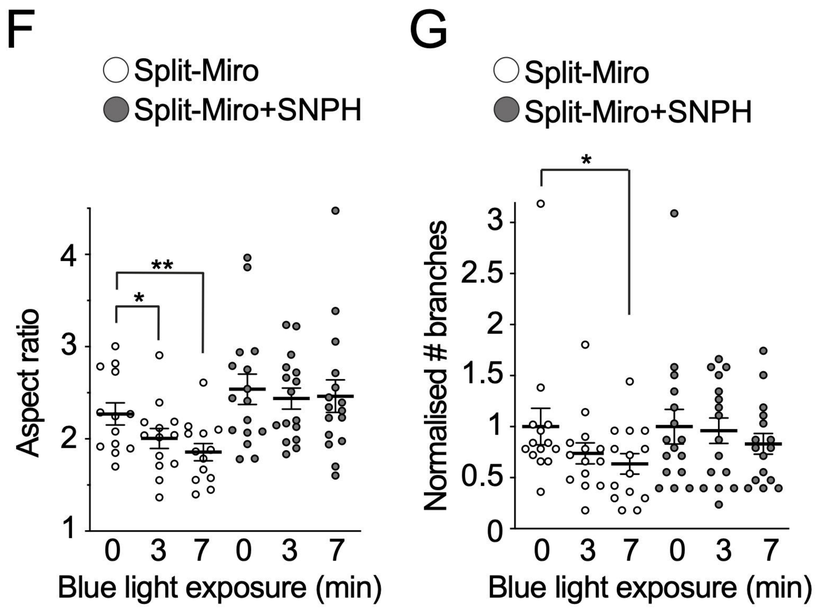

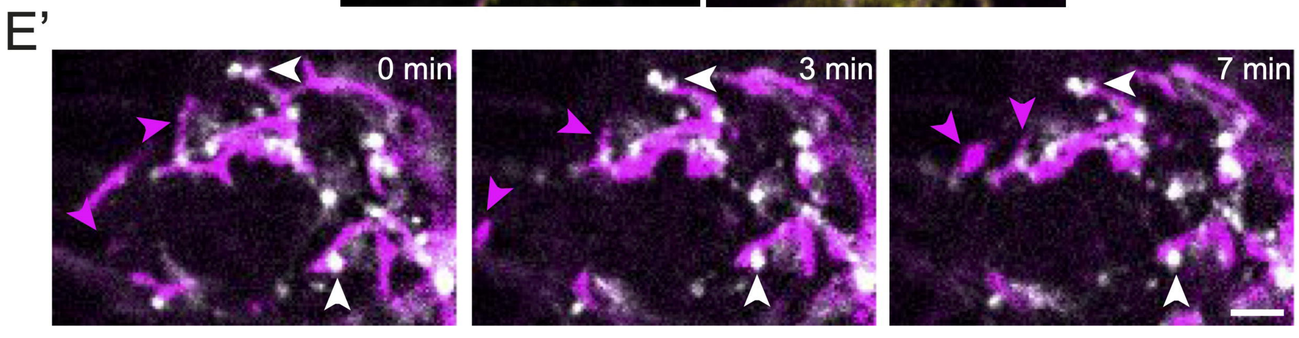

Figure 4

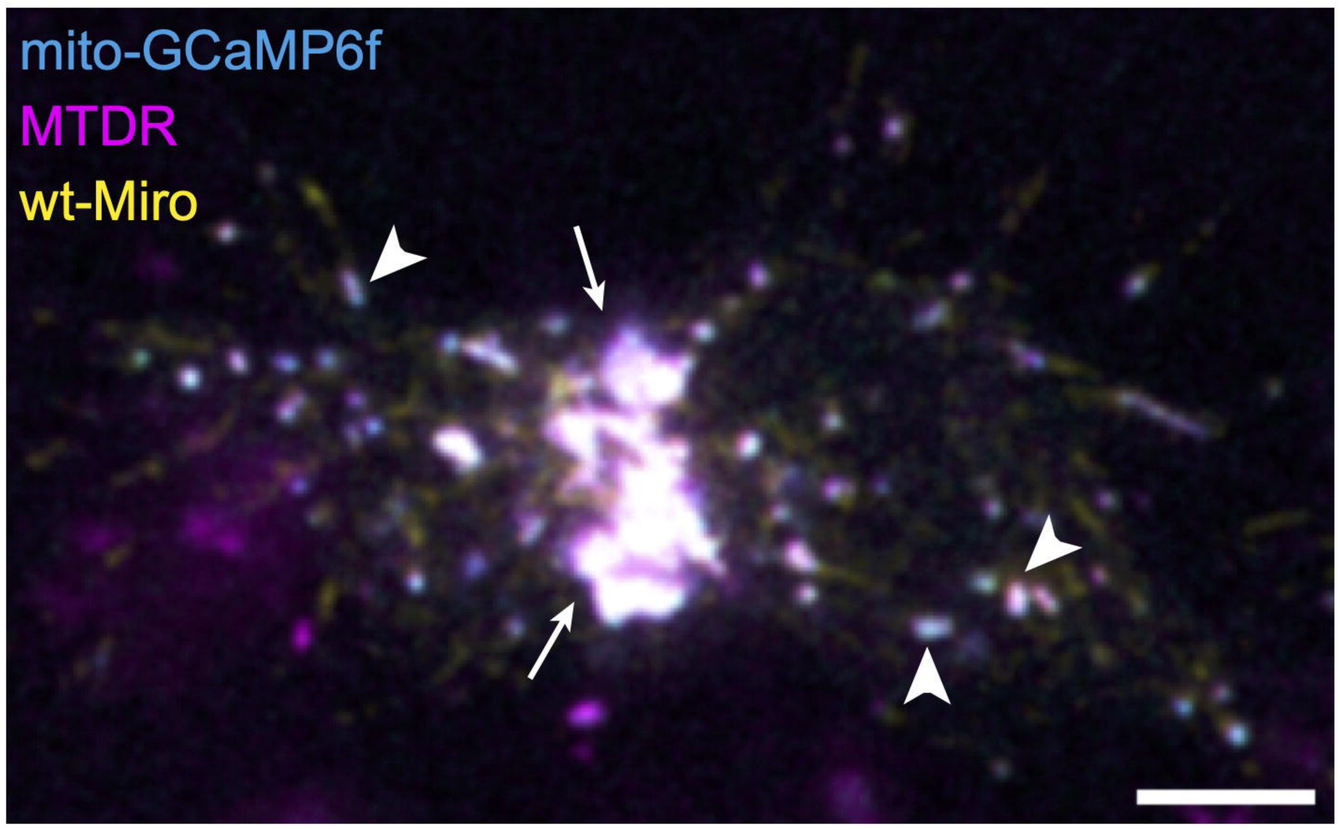

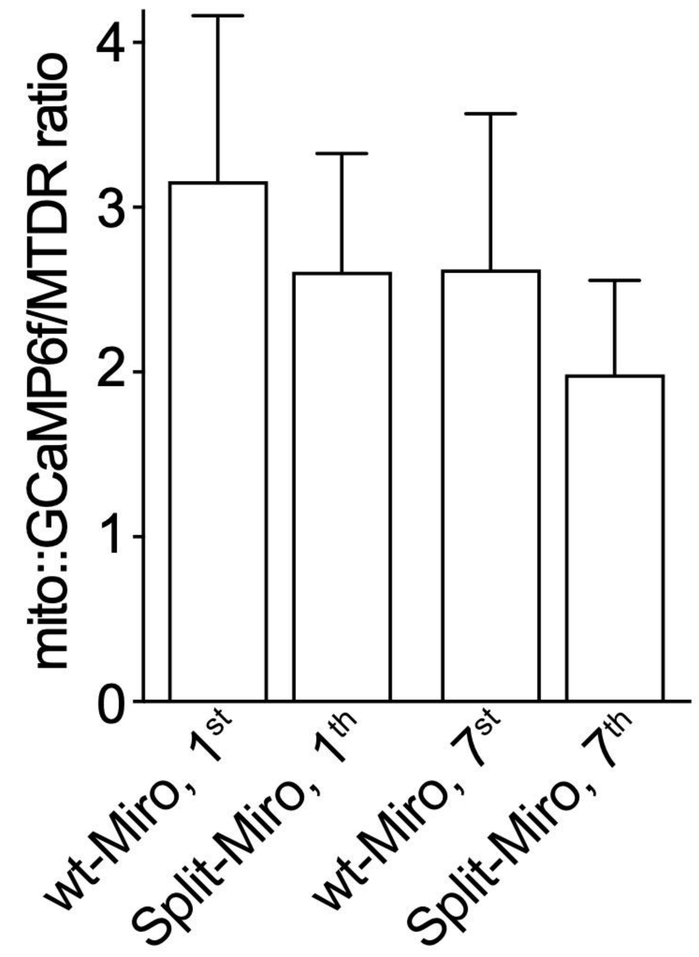

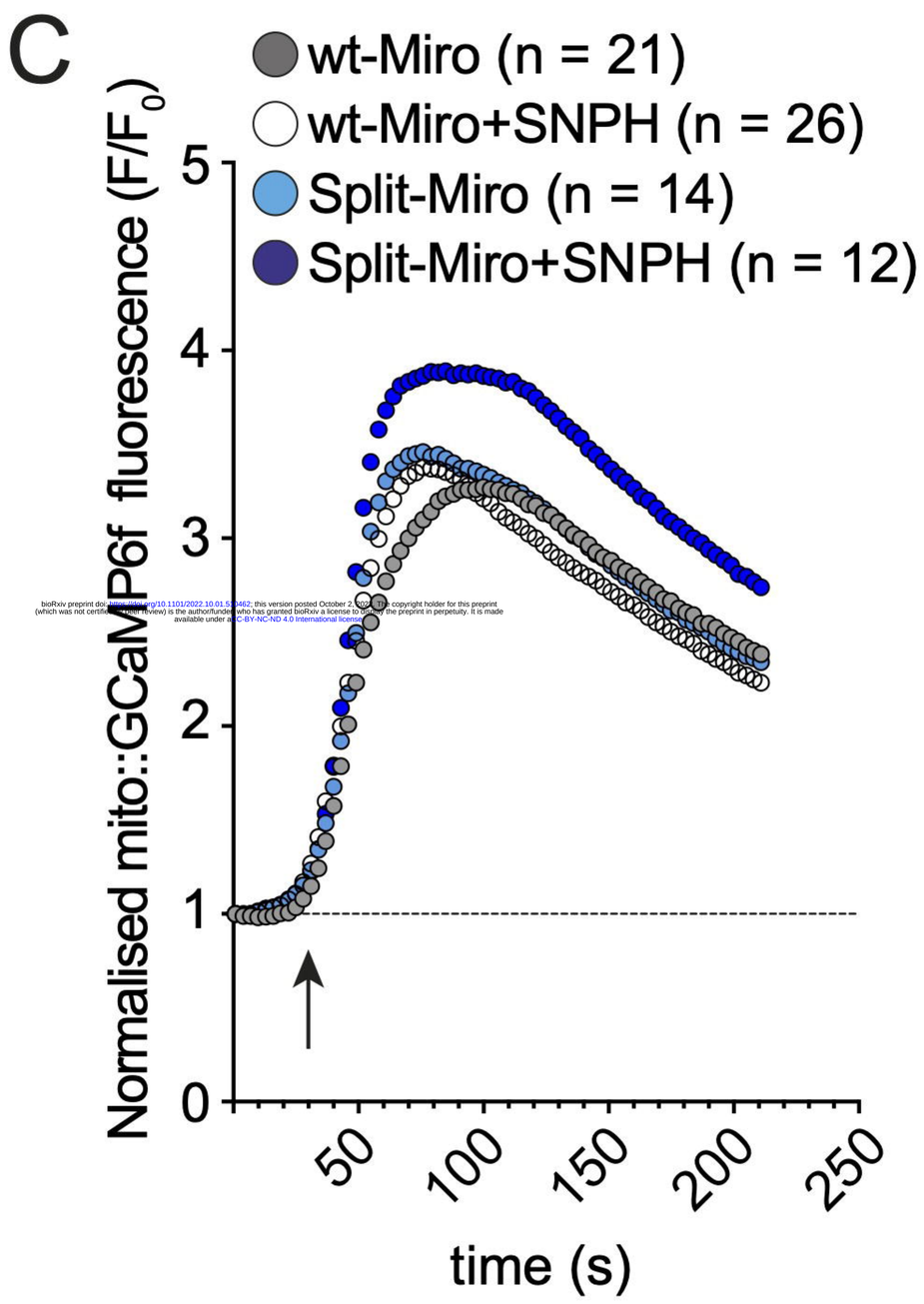

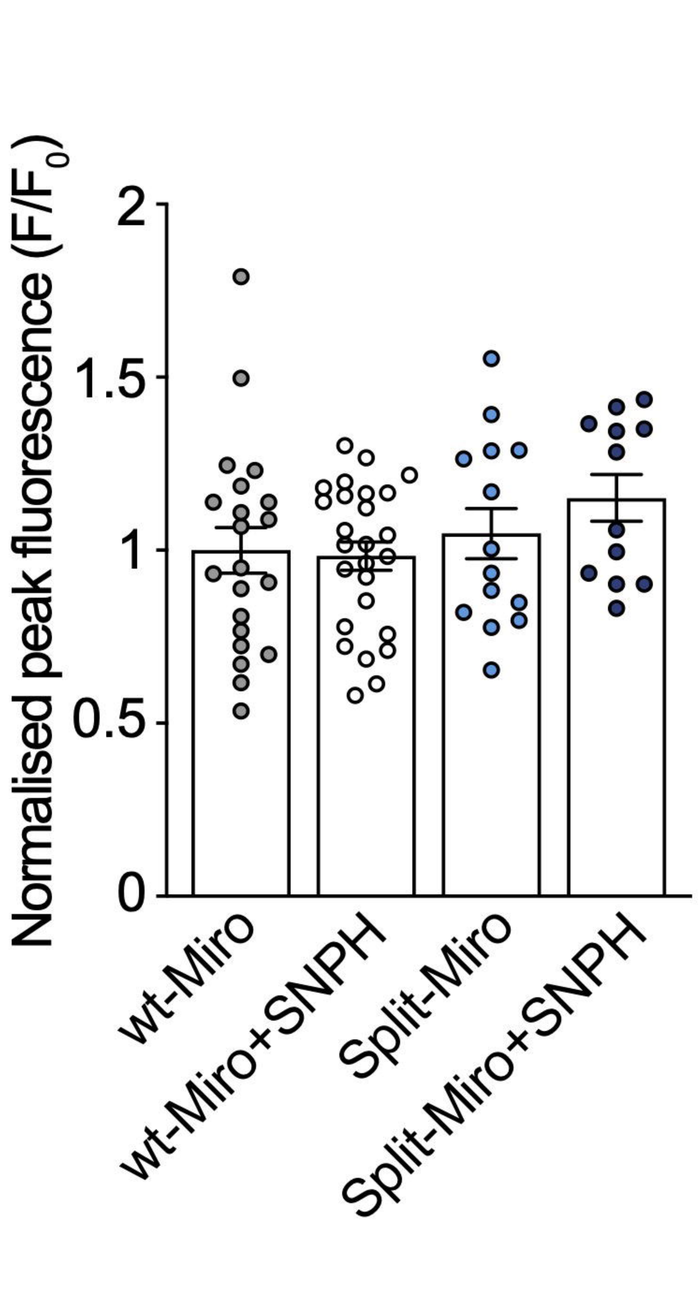

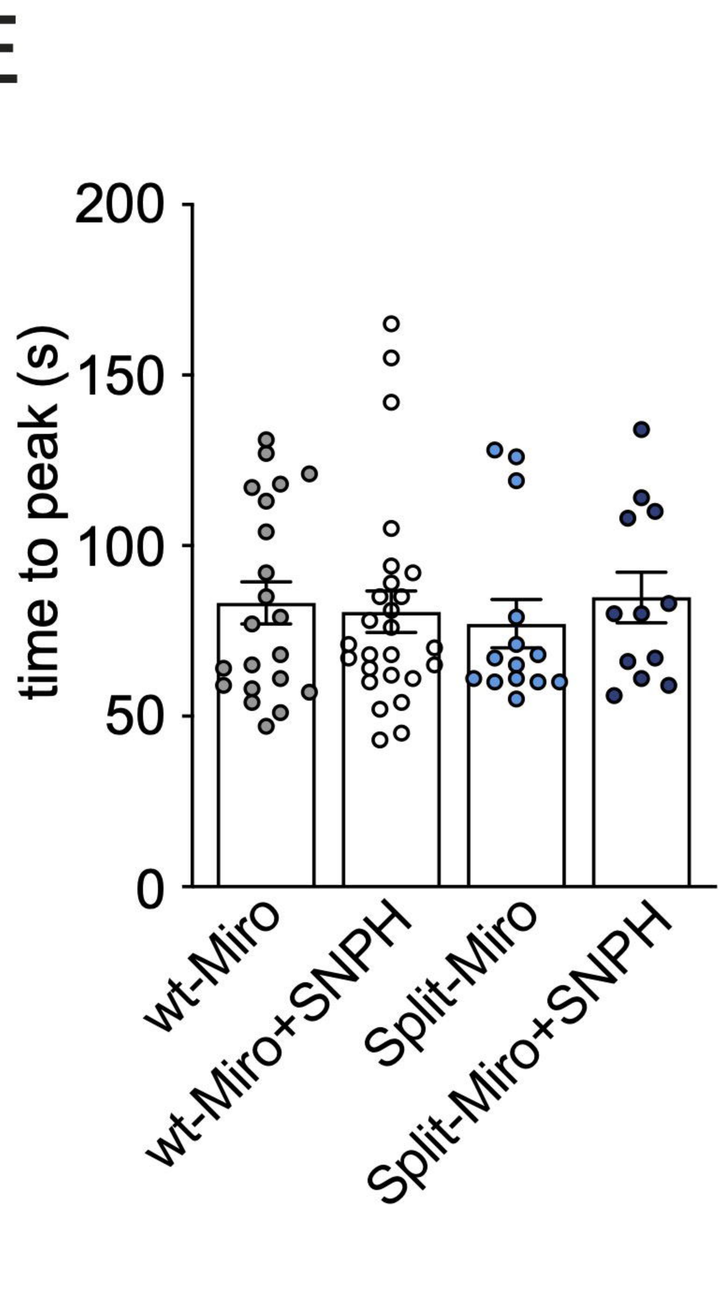

Figure 5

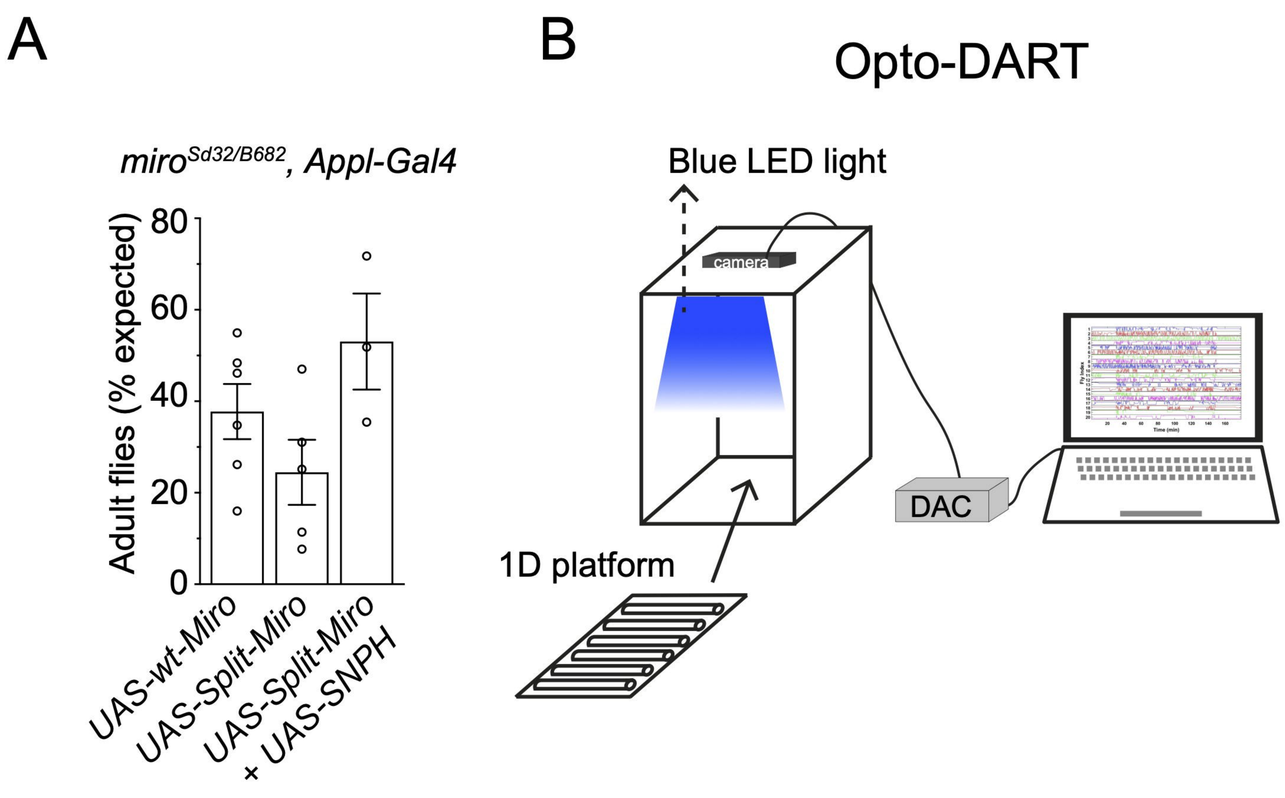
A
miroSd32/B682, Appl-Gal4
Adult flies (% expected)
0
20
40
60
80
UAS-wt-Miro
UAS-Split-Miro
UAS-Split-Miro
UAS-SNPH
×
B
Opto-DART
Blue LED light
camera
DAC
1D platform

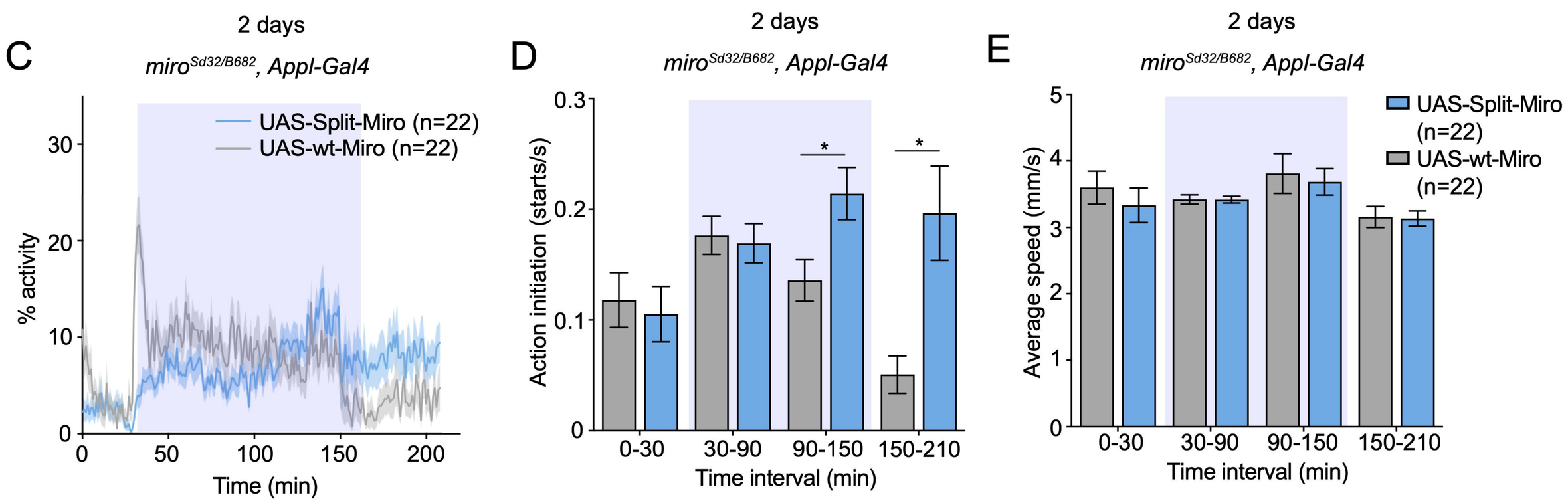
C
2 days
miroSd32/B682, Appl-Gal4
UAS-Split-Miro (n=22)
UAS-wt-Miro (n=22)
% activity
Time (min)
D
2 days
miroSd32/B682, Appl-Gal4
Action initiation (starts/s)
0-30
30-90
90-150
150-210
Time interval (min)
*
*
E
2 days
miroSd32/B682, Appl-Gal4
Average speed (mm/s)
UAS-Split-Miro (n=22)
UAS-wt-Miro (n=22)
Time interval (min)

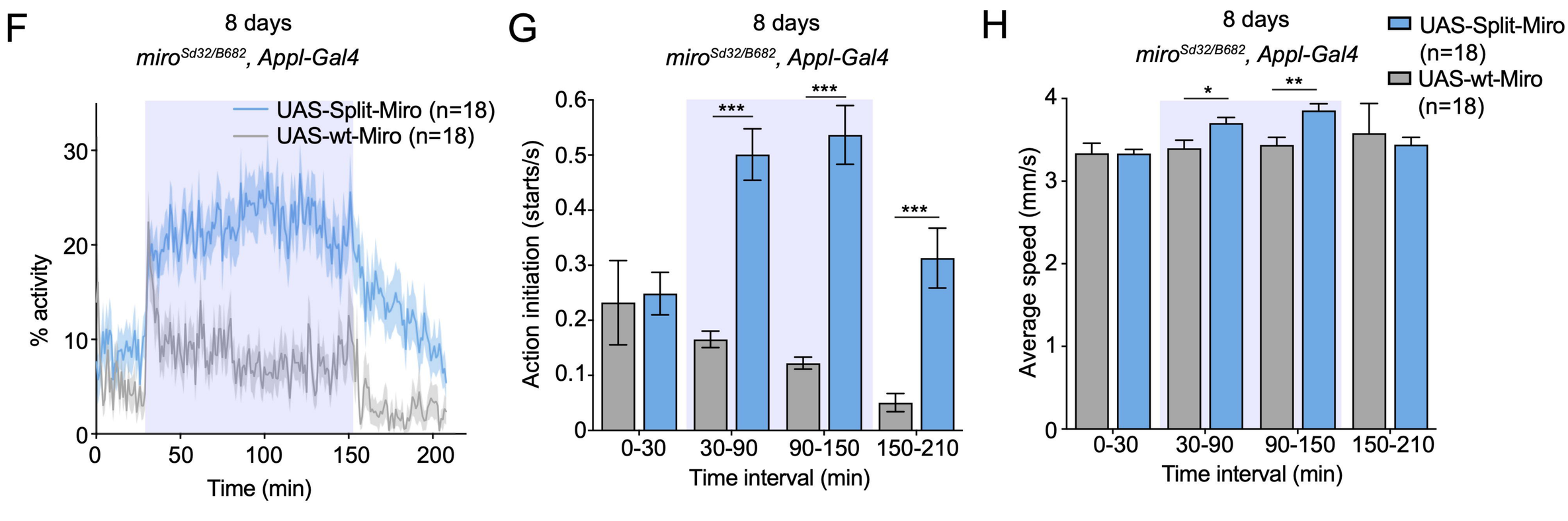
F
8 days
miroSd32/B682, Appl-Gal4
UAS-Split-Miro (n=18)
UAS-wt-Miro (n=18)
% activity
Time (min)
G
8 days
miroSd32/B682, Appl-Gal4
Action initiation (starts/s)
***
***
***
0-30
30-90
90-150
150-210
Time interval (min)
H
8 days
miroSd32/B682, Appl-Gal4
UAS-Split-Miro (n=18)
UAS-wt-Miro (n=18)
Average speed (mm/s)
*
**
Time interval (min)

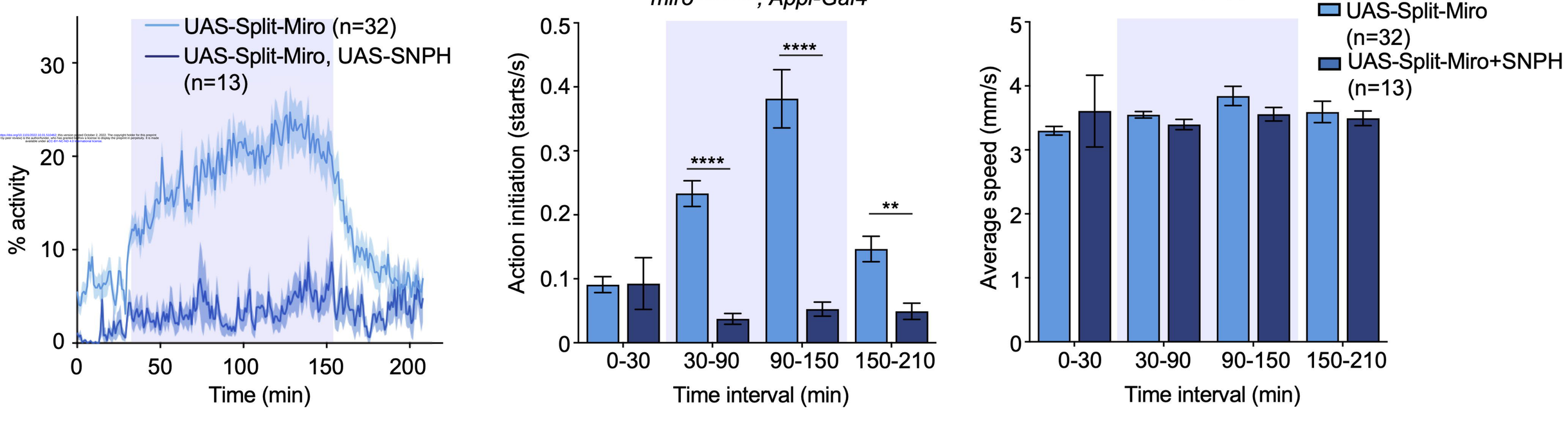
I
8 days
miroSd32/B682, Appl-Gal4
UAS-Split-Miro (n=32)
UAS-Split-Miro, UAS-SNPH (n=13)
% activity
Time (min)
J
8 days
miroSd32/B682, Appl-Gal4
Action initiation (starts/s)
****
****
**
0-30
30-90
90-150
150-210
Time interval (min)
K
8 days
miroSd32/B682, Appl-Gal4
UAS-Split-Miro (n=32)
UAS-Split-Miro+SNPH (n=13)
Average speed (mm/s)
Time interval (min)

Figure 6